MULTISCALE MODELING OF HEAT TRANSFER ENHANCEMENT WITH FIBER ARRAY INSERTS

By

ANDREW READ MARTIN

A DISSERTATION PRESENTED TO THE GRADUATE SCHOOL
OF THE UNIVERSITY OF FLORIDA IN PARTIAL FULFILLMENT
OF THE REQUIREMENTS FOR THE DEGREE OF
DOCTOR OF PHILOSOPHY

UNIVERSITY OF FLORIDA

1997

ACKNOWLEDGMENTS

Like many things in life, obtaining a Ph.D. degree is a task that cannot be accomplished singlehandedly. I am grateful to all of those persons who were directly or indirectly responsible in the production of this dissertation. Dr. C. Saltiel, who served as the Ph.D. committee chair, is to be thanked for his guidance, mentoring, and friendship over the years. The committee Cochair, Professor W. Shyy, lended a great deal of support and encouragement, and kept a watchful eye over me after Dr. Saltiel left Florida. Professors J. Klausner, W. Lear, and R. Mei, who compose the remainder of the Ph.D. committee, are also to be thanked for their expert advice and guidance. Many of the computer programs used in the course of this dissertation were obtained from other individuals, whom I would like to recognize: Professor J. Chai for the radiation program; Dr. M. Rao and Dr. H. Ouyang for fluid flow and heat transfer programs; and Dr. S. Thakur, Dr. H. S. Udaykumar, and Dr. J. Wright for the three-dimensional curvilinear program. Throughout the course of my studies, I had the privilege to work alongside numerous graduate student colleagues; the good times and friendships formed as a result will not be forgotten.

Finally, I express heartfelt gratitude to my American and Swedish families. This dissertation is dedicated to them. To my wife, Viktoria, I declare the following 'Norrlands' sentiment: 'Jag hoppas att det får duga.' (Translation from Swedish: 'I hope that this will do.')

TABLE OF CONTENTS

page

ACKNOWLEDGMENTS ii

NOMENCLATURE v

ABSTRACT ix

CHAPTERS

1 INTRODUCTION 1

1.1 Basic Features of Multiscale Modeling 2
1.2 Heat Transfer Enhancement and Fiber Array Concept 3
1.3 Scale Analysis of Flow and Heat Transfer in Fiber Arrays 8
1.3.1 Inertial Effects 8
1.3.2 Local Thermodynamic Equilibrium 11
1.3.3 Importance of Radiative Transfer 12
1.4 Contributions of Present Study 13

2 MICROSCOPIC AND MACROSCOPIC GOVERNING EQUATIONS . . 14

2.1 Microscopic Transport and Governing Equations 14
2.2 Volume Averaged Transport Equation and Macroscopic Equations . . 15
2.2.1 Macroscopic Conservation of Mass 17
2.2.2 Macroscopic Conservation of Momentum 18
2.2.3 Macroscopic Conservation of Energy 18
2.2.4 Macroscopic Radiative Transport 19
2.3 Treatment of Macroscopic Source Terms 22
2.3.1 Momentum Source Term 23
2.3.2 Energy Source Term 24
2.4 Summary of Macroscopic Governing Equations 25
2.5 Multiscale Modeling Approach 26
2.6 Numerical Modeling Considerations 27
2.6.1 SIMPLE Algorithm and Extension to Curvilinear Coordinates 28
2.6.2 Solution to the RTE 32

3 MICROSCALE MODELING OF FLUID FLOW AND HEAT TRANSFER IN SPARSE, PERIODIC CYLINDER ARRAYS 35

3.1 Longitudinal Flow 36
3.2 Transverse Flow 38
3.2.1 Problem Description and Numerical Approach 39
3.2.2 Results: Fluid Flow 45
3.2.3 Results: Heat Transfer 54

3.3 Yawed Flows 57
3.4 Concluding Remarks 60

4 CONVECTIVE AND RADIATIVE HEAT TRANSFER ENHANCEMENT WITH FIBER ARRAY INSERTS IN TUBE FLOW 62

4.1 Analysis 63
4.1.1 Momentum and Energy Source Terms 63
4.1.2 Radiative Transport 64
4.1.3 Numerical Approach 68
4.2 Results 71
4.3 Concluding Remarks 76

5 CONVECTIVE HEAT TRANSFER ENHANCEMENT WITH FIBER ARRAY INSERTS IN RECIRCULATING FLOWS 78

5.1 Problem Description and Numerical Approach 80
5.2 Results – Fluid Flow 84
5.3 Results – Heat Transfer 89
5.4 Concluding Remarks 95

6 CONCLUSIONS 97

REFERENCES 100

BIOGRAPHICAL SKETCH 105

NOMENCLATURE

a	insert length; SIMPLE algorithm coefficient; specific surface area
A	area; differencing function; first Ergun constant
b	correlation constant; source term
B	second Ergun constant
c	cylinder-to-cylinder distance
C	permeability parameter
C_a, C_s	absorption and scattering cross sections
c_p	specific heat
d	fiber diameter; SIMPLE algorithm coefficient
D	diffusion term; tube diameter
D_{cx}, D_{cy}	direction cosines
Da	Darcy number
$\vec{e}_x, \vec{e}_y, \vec{e}_z$	unit normal vectors
$E_f, \boldsymbol{E}_f$	energy equation source term scalar and tensor
f'	modified friction factor
F	convection term; Forchheimer constant
g	correlation constant
h	convective heat transfer coefficient
h_l	duct head loss
H	duct height
i, j	numerical indices
$I_\lambda, I_{b\lambda}$	spectral and blackbody radiative intensities
$\vec{J}_k$	conservation vector or tensor

$k, \boldsymbol{k}$	thermal conductivity scalar and tensor; complex index of refraction
$K, \boldsymbol{K}$	permeability scalar and tensor
L	tube or duct length
m	correlation constant
$M_f, \boldsymbol{M}_f$	momentum equation source term scalar and tensor
n	real index of refraction; correlation constant
$\vec{n}$	surface normal vector
N	number density
Nu	Nusselt number
p	pressure
P	Peclet number
$q, \vec{q}_R$	heat flux scalar and radiative heat flux vector
Q_a, Q_s	absorption and scattering efficiency factors
r	radial coordinate; correlation constant
Re_d	particle Reynolds number
Re_D	tube Reynolds number
Re_H	duct Reynolds number
$Re_{\sqrt{K}}$	Darcian Reynolds number
s	radiative path length
$\vec{s}$	direction vector
$S_k, \boldsymbol{S}_k$	source term scalar and tensor
T	temperature
u	axial velocity
U	average or characteristic velocity
$\vec{u}$	velocity vector
v	radial or transverse velocity
V	representative elementary volume (REV); contravariant velocity
$\vec{w}_k$	interfacial velocity vector

x, y, z	cartesian coordinates
x_R	size parameter
z	axial coordinate

Greek:

β_λ	spectral extinction coefficient
δ	distance between control volume centers
δ_m	maximum percent relative difference
ϵ	volume fraction
$\overline{\epsilon}_w$	wall emissivity
γ	circumferential coordinate
Γ	scalar or vector quantity
$\kappa_\lambda, \overline{\kappa}$	spectral and Planck-mean absorption coefficients
λ	wavelength
μ	dynamic viscosity
ω	wavenumber
Ω	solid angle
ϕ	azimuthal angle
ϕ_s	scattering angle
Φ_k	conservation variable
Φ_λ	scattering phase function
Ψ	yaw angle
ρ	density
σ	Stefan-Boltzmann constant
σ_λ	spectral scattering coefficient
θ	polar angle
Θ	heat exchanger effectiveness
τ_D	optical depth

Subscripts, superscripts, and other symbols:

b	bulk
c	centerline
e	east side; effective
E	east coefficient
f	fluid phase
fs	fluid-solid interface
h	homogeneous
i	inlet
k	phase
m	modified
n, N	north side and coefficient
nb	neighbor coefficient
p, P	central location and coefficient
r	reference
R	radiative
s	solid phase; south side
S	south coefficient
w	wall; west side
W	west coefficient
$*$	nondimensional quantity; previous value
$'$	correction
$''$	microscopic dispersion
$\mathcal{O}(\,)$	order of magnitude
$\langle\,\rangle$	volume averaging operator

Abstract of Dissertation Presented to the Graduate School
of the University of Florida in Partial Fulfillment of the
Requirements for the Degree of Doctor of Philosophy

MULTISCALE MODELING OF HEAT TRANSFER ENHANCEMENT WITH FIBER ARRAY INSERTS

By

Andrew Read Martin

December 1997

Chair: Craig J. Saltiel
Major Department: Mechanical Engineering

The overall objective of this investigation is to analyze fiber array inserts for internal heat transfer enhancement. A numerically-based multiscale modeling procedure is employed to determine the complex flow field characteristics. In the fiber array insert technique, an array of small diameter fibers ($\sim 100\mu$m) is placed within an externally heated duct. Heat transfer augmentation may result from radiative exchange between duct walls and insert, convection from insert to fluid, and alterations in the flow field. Silicon carbide is selected as the fiber material for its durability, high thermal conductivity, and radiative characteristics.

Before the performance of the inserts is assessed, an analysis of flow in sparse, periodic cylinder arrays is conducted. The present investigation focuses on laminar cross flow in square and triangular arrays, with porosities ranging from 0.80 to 0.99 and cylinder Reynolds numbers varying from about 3 to 160. Frictional losses are shown to follow Darcy's law when the Darcian Reynolds number is of the order one, while significant non-Darcy effects are seen at higher Reynolds numbers. Power-law relationships for frictional losses and Nusselt number are shown to correlate well with detailed simulation results.

Square array inserts with porosities greater than 0.90 are considered as the enhancement device. In the first application, inserts are aligned longitudinally in a circular tube under laminar flow conditions. Results show that inserts increase heat transfer largely by radiation, with significant augmentation shown for porosities as high as 0.99. In recirculating flow situations, the laminar flow field downstream of a backward-facing step is greatly influenced by transverse inserts that partially fill the duct. Performance deteriorates with short and highly porous inserts, but enhancement caused by longer and less porous inserts yields a 30% reduction in wall temperature. For both applications, frictional losses rise monotonically as the porosity is reduced. Non-Darcy flow is most appreciable in the backward-facing step application, and deviation from local thermodynamic equilibrium is most apparent in the tube flow application, where radiation is important. With careful design, fiber array inserts show great potential as a heat transfer enhancement technique.

CHAPTER 1
INTRODUCTION

Enhancing heat transfer is a major design objective for engineers in the chemical, power, aerospace, and transportation industries. A number of goals can be achieved by increasing heat transfer: (a) reduced heat transfer areas; (b) increased process efficiency; and (c) operation at lower temperatures. Goal (a) is of prime importance in applications where heat exchanger size is limited, such as in air conditioning and refrigeration units, automobiles and trucks, and space heaters. Goal (b) is an important objective in almost all thermal processes, but can be especially critical in determining the cost-effectiveness of a process in an industrial setting. The last goal relates to cases where equipment lifetime becomes compromised due to adverse operating conditions. For example, durability is a vital issue for equipment operating under highly corrosive conditions, such as in coal-fired boilers or waste-to-energy incinerators, where losses to corrosion are magnified by excessive operating temperatures [34, 47, 56]. Since corrosion of metals is very sensitive to temperature [47], even small increases in heat transfer rates can greatly lengthen equipment lifetime by reducing corrosion losses.

In the search for new, more effective heat transfer enhancement techniques, computational fluid dynamics (CFD) continues to play an important role. While advances in computational capabilities and CFD methods have allowed researchers to analyze a vast number of applications, the evaluation of certain classes of flows remains problematic. For instance, the direct simulation of flows in complex microscopic geometries such as porous media is difficult or impossible to analyze by standard CFD approaches. As an alternative, separate computations can be performed

at microscopic and macroscopic levels, provided that some means of linking these scales can be found; this is the essence of multiscale modeling. Multiscale modeling strikes a balance between numerical accuracy and computational practicality, and it is an indispensable tool in the study of heat transfer enhancement.

This chapter contains a general outline of multiscale modeling and presents some more details of heat transfer enhancement. The specific heat transfer enhancement device under consideration, fiber array inserts, is also described.

1.1 Basic Features of Multiscale Modeling

Situations which feature complicated microscale geometries can be classified as flows through porous media. In porous media flow, liquids and/or gases move through complex networks of channels or interstices, which are composed of a solid matrix. A broad range of applications exist for porous media flows: aquifers, oil reservoirs, and other naturally occurring formations; packed beds and variety of electrical and thermal equipment; and insulation systems [4, 6, 12]. Even in cases where the geometry of the porous media is well ordered, the solution of the microscopic transport equations in such a tortuous structure is formidable. Volume averaging of the microscopic transport equations may be used to simplify the treatment of the complex features. The resulting macroscopic equations contain source terms which represent the influence of microscopic flow phenomena on the large-scale features. Evaluation of these source terms can be handled with CFD by performing microscopic flow analyses, which are then integrated into the macroscopic computations.

Figure 1.1 schematically illustrates the concept of multiscale modeling. The macroscopic domain consists of a porous media where the detailed structural properties are essentially smoothed out. From an engineering point of view, it is important to determine average properties such as bulk fluid temperature and pressure drop, with the detailed characteristics being of little concern. Of course, the microscopic and macroscopic flows are interdependent, so it is necessary to consider

analyses at the microscale level. If a portion of the macroscopic domain is magnified (see Figure 1.1), details of the microscale can be seen. Assuming that the porous media can be exactly described at every location, it is possible to isolate a small section of the microstructure where the microscopic flow equations may be applied. For cases where the porous media is ordered, as shown in Figure 1.1, the additional assumption of microscopically fully developed flow (i.e. periodic conditions) allows for the microscale analyses to be performed for a single representative elementary volume (REV). If the flow is not periodic, multiple calculations would have to be performed over a number of REV's which characterize the microscale flow. Whatever the case may be, microscale computations that are performed over the REV(s) must be linked to the macroscopic flow field in some manner. One approach is to directly couple microscopic and macroscopic calculations, using some form of iteration to arrive at the ultimate solution. Alternatively, microscale computations can be independently performed over a previously determined range of parameters. Correlations featuring the macroscopic variables can be then developed and applied to the problem at hand. This uncoupled multiscale modeling approach is taken for the present investigation, and the specific details are included subsequently.

1.2 Heat Transfer Enhancement and Fiber Array Concept

As mentioned in the opening section of this chapter, the goal of temperature reduction is often an important design criteria for the minimization of corrosion. This specific goal is selected as the primary motivation for heat transfer augmentation. The corrosion process is a complex phenomena, and greatly depends upon factors such as the shape and composition of the metal, its service history, and environmental conditions [47]. One type of corrosion that is encountered in many heat exchanger applications is attack by oxidative gases. For example, hot flue gases which pass through a boiler or furnace oxidize metal components such as water wall tubes and superheaters. Since it is usually not possible to alter the composition

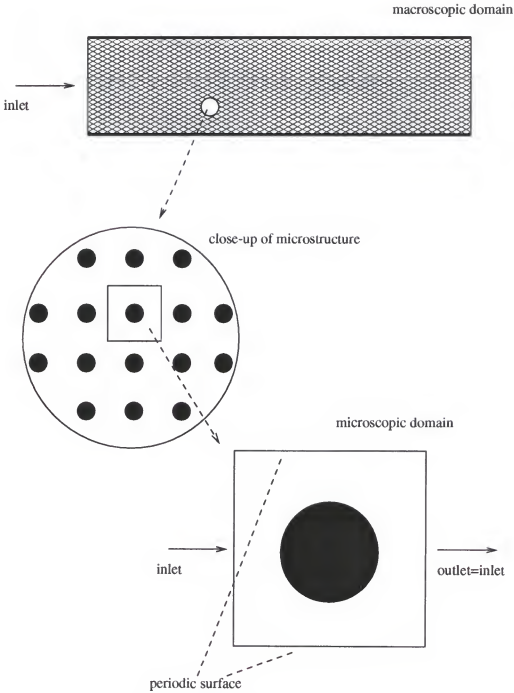

Figure 1.1: Schematic of multiscale modeling approach.

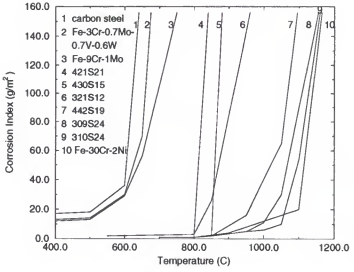

Figure 1.2: Corrosion index versus temperature for various steel alloys (from Shreir [47]).

of the flue gas constituents, other steps must be taken to reduce corrosion, hence the importance of heat transfer enhancement. Figure 1.2 illustrates the role of temperature in the corrosion of various steel alloys. The curves shown in this figure were generated from experimental data, whereby small cylindrical specimens were intermittently exposed to a flue gas stream at a specific temperature over a period of about four days. Specimens were weighed at various intervals, and the subsequent weight gain due to corrosion was used to determine the corrosion index (measured in units of g/m^2). It can be seen that the corrosion index increases exponentially for each steel alloy around a critical temperature; for instance, carbon steel shows extreme sensitivity to temperature just above 600 C for these experiments. Although the rate of corrosion will not be the same for other oxidative conditions, the trends shown in Figure 1.2 clearly demonstrate that once a threshold temperature level is attained, even marginal reductions in temperature can significantly impact corrosion.

Methods for increasing heat transfer are ordinarily aimed at those fluid streams which present the greatest thermal resistance. In many heat exchange devices, the internal flow stream has a lower heat transfer coefficient, and thus limits the total heat transfer rate. For instance, the operational efficiency of fluidized bed combustors and fuel-fired boilers is largely dependent on the heat transfer coefficients present on the tube-side, or internal, flow stream. In cases where outside heat transfer rates are lower than the internal rates, considerations governing the nature of the flow stream, such as pressure loss and erosion/corrosion, limit measures by which heat transfer may be increased. Thus, in many instances the only available option is to increase internal heat transfer if total heat transfer is to be augmented.

A number of heat transfer augmentation devices are available to increase internal heat transfer. Extended surfaces, such as fins, coils, or baffles, can be used to increase the effective surface area, which allows for better contact between the heat exchanger and the fluid [7]. Surface roughening and swirl-flow devices can be used to change the nature of the flow or to promote turbulence, resulting in heat transfer enhancement [7]. In situations where radiation is not an effective heat transfer mode, which arise when the fluid is transparent to thermal radiation, the fluid can be made radiatively participating by dispersing solid particles in the micron to millimeter size range. This method has been considered for enhancing heat transfer in gas turbines, nuclear reactors, fluidized beds, and space power generation systems [7]. Particle-surface radiation is especially effective at high temperatures, where heat transfer coefficients have been improved by as much as a factor of 20 [7]. In addition, pressure losses are minimal when the volume fraction of solid particles is low. For cases where particles may damage equipment, methods are required to fix solid components within the flow path. A number of studies have examined radiative enhancement using packed or fluidized beds [17, 18, 58]. These techniques are characterized by either large particle sizes or large solid volume fractions, resulting

in unacceptable pressure losses for fluid velocities typical of many heat transfer systems.

Recent investigations have focused on the use of porous media inserts in order to obtain heat transfer enhancement with a minimum of frictional losses. In applications where temperatures are sufficiently large so that radiation is an important heat transfer mode, Im and Ahluwahlia [31] proposed the use of longitudinally-aligned fiber arrays in tube flow, while Zhang et al. [68] explored coaxial ceramic inserts. Other researchers have investigated the use of strategically located porous segments for heat transfer enhancement. Huang and Vafai [29] studied flow in a two-dimensional duct with intermittently placed porous blocks located on one of the walls, and in a related study, Vafai and Huang [61] considered these blocks to be imbedded within the duct walls. Abu-Hijleh [1] investigated flow over a backward-facing step where part of the downstream duct wall was porous. While the above studies demonstrate the possible gains in heat transfer with porous inserts, they do not address situations where the flow is inherently recirculating in the absence of the insert. Hendricks et al. [27] experimentally investigated the use of brush inserts within a complex cooling passage for the mitigation of flow separation and augmentation of local heat transfer. In addition, Ichimiya et al. [30] numerically evaluated the use of porous media in a miter bend.

It is clear from these studies that porous inserts offer great potential for heat transfer augmentation. Of the many possible porous insert configurations, fiber arrays are selected as a candidate technique, as shown in Figure 1.3. As shown in the figure, the fiber array may be installed either longitudinal or transverse to the streamwise flow direction, depending upon the desired heat transfer objectives. Longitudinal orientation is favorable where wall-to-fiber radiation is expected to be important, presuming that the fiber material has good radiative characteristics. On the other hand, transverse orientation allows for additional heat transfer by conduction from the wall to the fiber array. In addition, the spacing arrangement

between adjacent fibers can vary, but for this study only square and triangular arrays are considered, shown in Figure 1.3(c). (It is recognized that actual fiber array inserts may be non-uniform or may require cross-wires for support, but such aspects are not accounted for here.) Since frictional losses should be as low as possible, high porosity fiber arrays are examined, which have fiber-to-fiber distances greater than two times the fiber diameter. For this investigation, silicon carbide (SiC) is chosen as the fiber material with a commercially available size (150μm diameter [15]). Silicon carbide has a number of characteristics which make it an excellent material: high tensile strength [15, 42]; strong resistance to high temperatures and oxidation [15, 41]; high thermal conductivity; and good radiative properties [31]. Ultimately, the overall impact of the fiber array on the heat transfer and frictional losses depends upon the orientation, fiber size and material, and number of fibers employed.

1.3 Scale Analysis of Flow and Heat Transfer in Fiber Arrays

Scale analysis, also referred to as order-of-magnitude analysis, is an indispensable tool for many engineering calculations, as it can highlight some of the more important features of complex problems. In the following sections, scale analysis is used to characterize flow and heat transfer in fiber arrays for heat transfer enhancement.

1.3.1 Inertial Effects

Historically, the flow of fluids through porous media has been described by Darcy's law [6], named after the 19th century French engineer who studied water flowing through fountains. Although empirical in nature, Darcy's law has been successfully used in a broad range of porous media flows. Darcy's law may be stated as follows:

$$-\nabla\langle p_f\rangle^f = \frac{\mu_f}{K}\langle U_f\rangle \tag{1.1}$$

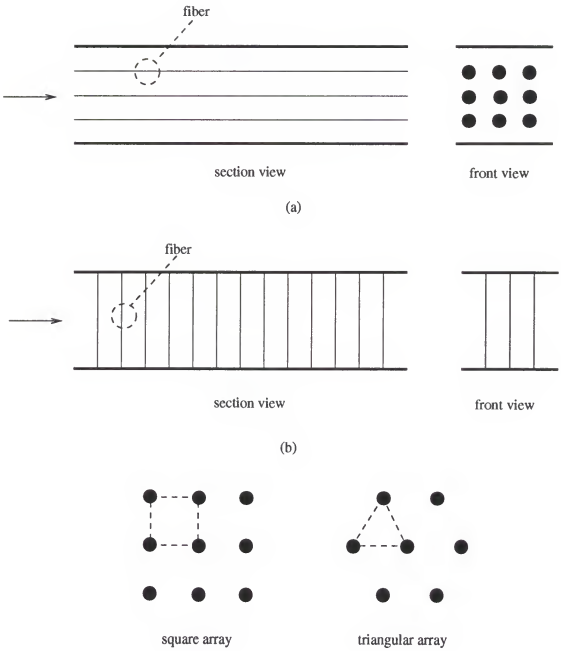

Figure 1.3: Schematic of fiber array concept – (a) longitudinal orientation; (b) transverse orientation; (c) square and triangular arrays.

where $-\nabla\langle p_f\rangle^f$ is the pressure gradient, μ_f is the fluid dynamic viscosity, $\langle U_f\rangle$ is the characteristic velocity, and K is the permeability of the porous media. Angle brackets have been used to denote the volume averaging operation, which will be discussed in a later chapter. The square root of the permeability, $\sqrt{K}$, has units of length and can be taken as a characteristic dimension of the pore size [6]. Hence, the Darcian Reynolds number, $Re_{\sqrt{K}}$, may be used to characterize flows in porous media:

$$Re_{\sqrt{K}} = \frac{\rho_f \langle U_f\rangle \sqrt{K}}{\mu_f} \tag{1.2}$$

where ρ_f is the fluid density. If the flow is slow, K is a function only of the porosity and geometry of the porous media, and hence Darcy's law may be employed. However, inertial effects and/or turbulence causes the permeability to be dependent upon the flowrate. This condition is known as non-Darcy flow, which becomes important when $Re_{\sqrt{K}}$ is of order one or greater [6].

In order to determine the importance of non-Darcy flow in fiber array inserts, the macroscopic Reynolds number, Re_D, may be specified, where

$$Re_D = \frac{\rho_f \langle U\rangle D}{\mu_f} \tag{1.3}$$

The length variable D represents the hydraulic diameter of the macroscopic domain. For this analysis, Re_D is taken to be of order 10^3, typical of a high Reynolds number, but laminar, flow. Considering a gas such as air at standard conditions, setting D to order 10^{-2} m allows for the determination of the characteristic velocity from Equation (1.3), which results in order 10^0 m/s. In a later chapter, it will be shown that $\sqrt{K}$ is of order 10^{-4} m for fiber array inserts with high porosity and small diameter ($\sim 100\mu$m). Hence, under these conditions the order of $Re_{\sqrt{K}}$ is 10^1, showing that non-Darcy effects may be evident here.

1.3.2 Local Thermodynamic Equilibrium

With respect to heat transfer in porous media, the condition of local thermodynamic equilibrium (LTE) assumes that the porous media and the fluid are isothermal within the REV. (In other contexts, the term 'LTE' refers to equilibrium between internal energy storage modes at the molecular level, which is assumed to be valid in this study. While these separate LTE definitions are somewhat contradictory, the former statement is taken in order to maintain consistency with usage in the porous media literature.) Although this assumption is often taken in the study of porous media, LTE may not be valid for the fiber array inserts to be considered. Considering flow and heat transfer in the fiber array inserts shown in Figure 1.3(a) and (b), heat supplied by the duct walls is transferred to the fluid by conduction and convection. If the insert is in contact with the walls, heat is transferred to the fibers via conduction, otherwise conduction heat transfer within the insert is driven by a longitudinal difference in temperature. There is also the possibility of radiative exchange between the insert and the duct walls. Thus, both the fluid and the insert exchange heat with the duct walls; but coupled with this process is the insert-to-fluid transfer. Clearly, the quantitative description of such a complicated process is not an easy task, but scale analysis can nevertheless be instructive in ascertaining the importance of the LTE assumption.

Taking the transverse insert as an example, and neglecting radiative effects, suppose that the duct walls supply heat with a constant heat flux, q_w. A local energy balance at the duct walls shows that the wall heat flux must be balanced by conduction; that is

$$q_w = -k\frac{\partial T}{\partial y} \tag{1.4}$$

where k is the conductivity and y is the normal component to the wall. Heat is transferred by conduction through the fluid and also through the fibers for the transverse insert. Hence, the rate of conduction heat transfer from the wall to fluid

must be equal to the rate from the wall to the insert:

$$-k_f \frac{\partial T_f}{\partial y} = -k_s \frac{\partial T_s}{\partial y} \tag{1.5}$$

where subscripts f and s represent the fluid and insert, respectively. Assuming that the wall temperature T_w is constant over a small segment, a scale analysis performed on the above energy balance yields

$$-k_f \frac{T_w - T_f}{\Delta y} \sim -k_s \frac{T_w - T_s}{\Delta y} \tag{1.6}$$

Since the scale of Δy is the same for both phases, this relationship may be rearranged as follows:

$$\frac{T_w - T_f}{T_w - T_s} \sim \frac{k_s}{k_f} \tag{1.7}$$

Hence, if the two phases have disparate values of thermal conductivity, scale analysis shows that deviations from LTE may occur.

1.3.3 Importance of Radiative Transfer

In order to evaluate radiative transfer effects, the magnitude of radiative transfer may be compared to convective heat transfer from the insert to the fluid. The radiative heat flux, q_R, may be written in an order-of-magnitude sense as follows [39, 51]:

$$q_R \sim \sigma \left(T_r^4 - T_s^4 \right) \tag{1.8}$$

In this expression, σ is the Stefan-Boltzmann constant, and T_r is the reference temperature. The order of magnitude for each of these terms, denoted $\mathcal{O}(\ )$, is as follows: $\sigma \sim \mathcal{O}(10^{-8})$ W/m^2-K^4; and $(T_r^4 - T_s^4) \sim ((800 \text{ K})^4 - (750 \text{ K})^4) \sim \mathcal{O}(10^{11})$ K^4. (With the reference temperature taken at 800 K, which is a realistic value for high temperature applications, any difference in temperature greater than 50 K results in $(T_r^4 - T_s^4) \sim \mathcal{O}(10^{11})$ K^4.) The convective heat flux, q_c, between the insert and the fluid is found via Newton's law of cooling,

$$q_c \sim h \left(T_s - T_f \right) \tag{1.9}$$

where h is the convective heat transfer coefficient. Deviations from LTE are presumed to occur, resulting in an assumed temperature difference $(T_s - T_f) \sim \mathcal{O}(10^1)$ K. Furthermore, h is taken to have order 10^2 W/m^2-K, a value typical for gases [32]. Hence, the ratio of radiative to convective heat transfer is computed as

$$\frac{q_R}{q_c} \sim \frac{\sigma\left(T_r^4 - T_s^4\right)}{h\left(T_s - T_f\right)} \sim \mathcal{O}(10^0) \tag{1.10}$$

showing that both modes of heat transfer have equal importance for these conditions.

1.4 Contributions of Present Study

The overall objective of this investigation is to explore heat transfer enhancement with fiber array inserts using a multiscale modeling procedure. In order to accomplish this goal, the following topics are presented in this investigation:

- Governing equations for microscopic and macroscopic flow and heat transfer are presented, with a detailed discussion on the treatment of source terms.
- A microscopic analysis of fluid flow and heat transfer in sparse, periodic cylinder arrays is conducted. Key issues involved with this analysis include high porosities, inertial effects, and the relaxation of the LTE assumption.
- Fiber array inserts, aligned longitudinally to the flow stream in a circular pipe, are investigated for heat transfer enhancement and pressure loss characteristics. Nongray radiative transfer is included in this analysis.
- In addition, fiber array inserts are considered for the modification of an otherwise recirculating flow field. Similarly, heat transfer and frictional penalty are determined based on the number of fibers and the size of the insert.
- For both of the fiber array applications, the importance of microscale inertial effects and the LTE assumption is assessed.

CHAPTER 2
MICROSCOPIC AND MACROSCOPIC GOVERNING EQUATIONS

This chapter provides the analytical foundation necessary in the evaluation of fiber array inserts for heat transfer augmentation. The microscopic governing equations are first presented, and are subsequently volume averaged to produce the macroscopic equations. Treatment of source terms arising from the averaging process is discussed in detail.

2.1 Microscopic Transport and Governing Equations

The governing equations for continuity, momentum, and energy of a fluid at the microscopic level are well known to engineers and can be found in a number of references, such as Bird et al. [8]. To begin with, the general microscopic transport equation written for phase k of conservation variable Φ_k is written below [8]:

$$\frac{\partial \Phi_k}{\partial t} + \nabla \cdot (\Phi_k \vec{u}_k) = \nabla \cdot \vec{J}_k + \boldsymbol{S}_k \tag{2.1}$$

In this expression, $\vec{u}_k$ is the velocity vector, $\vec{J}_k$ is a vector or tensor one order greater than Φ_k, and $\boldsymbol{S}_k$ is the source term tensor. For flows in porous media, two phases are considered: fluid phase f; and solid phase s. The steady state, laminar flow formulation of the microscopic governing equations for an incompressible, Newtonian fluid with negligible body forces results in the following equations (continuity, momentum and energy):

$$\nabla \cdot \vec{u}_f = 0 \tag{2.2}$$

$$\rho_f \vec{u}_f \cdot \nabla \vec{u}_f = -\nabla p_f + \mu \nabla^2 \vec{u}_f \tag{2.3}$$

$$\rho_f c_{p,f} \nabla \cdot T_f \vec{u}_f = k_f \nabla^2 T_f \tag{2.4}$$

In the above, ρ_f is the fluid density, p_f is the fluid pressure, μ_f is the fluid dynamic viscosity, $c_{p,f}$ is the fluid specific heat, T_f is the fluid temperature, and k_f is the fluid thermal conductivity. These equations are also applicable for the solid phase; however, the continuity and momentum equations are not required if the solid is stationary, is non-deformable, and there is no mass transfer between phases. The energy equation for the solid phase is

$$0 = k_s \nabla^2 T_s - \nabla \cdot \vec{q}_R \tag{2.5}$$

where k_s is the solid phase conductivity, T_s is the solid temperature, and $\nabla \cdot \vec{q}_R$ is the divergence of the radiative heat flux. (Radiative transfer is discussed in a subsequent section.)

2.2 Volume Averaged Transport Equation and Macroscopic Equations

Before the volume averaged transport equation in conservative form is derived, a few definitions need to be stated. The total volume average of any scalar or vector quantity Φ_k, associated with phase k, is defined as

$$\langle \Phi_k \rangle = \frac{1}{V} \int_V \Phi_k dV \tag{2.6}$$

where V is the representative elementary volume (REV). (It is understood that Φ_k is zero in regions not occupied by phase k.) The intrinsic volume average is defined as

$$\langle \Phi_k \rangle^k = \frac{1}{V_k} \int_{V_k} \Phi_k dV \tag{2.7}$$

and may be related to the total volume average by

$$\epsilon_k \langle \Phi_k \rangle^k = \langle \Phi_k \rangle \tag{2.8}$$

where ϵ_k is the the volume fraction of phase k. The following theorems will also be invoked in the volume averaging of the transport equation [26, 52, 67]:

- The volume average of the time derivative is related to the time derivative of the volume average by

$$\left\langle \frac{\partial \Phi_k}{\partial t} \right\rangle = \frac{\partial \langle \Phi_k \rangle}{\partial t} + \frac{1}{V} \int_{A_k} \Phi_k \left(\vec{w}_k \cdot \vec{n}_k \right) dA \tag{2.9}$$

where A_k is the interfacial surface area, $\vec{w}_k$ is the interfacial velocity with respect to the global coordinate system, and $\vec{n}_k$ is the outward facing normal at the interface.

- The volume average of the gradient of Φ_k is related to the gradient of the volume average of Φ_k by

$$\langle \nabla \Phi_k \rangle = \nabla \langle \Phi_k \rangle + \frac{1}{V} \int_{A_k} \Phi_k \vec{n}_k dA \tag{2.10}$$

Likewise, the volume average of the divergence of $\vec{\Phi}_k$ is related to the divergence of the volume average of $\vec{\Phi}_k$ by

$$\langle \nabla \cdot \vec{\Phi}_k \rangle = \nabla \cdot \langle \vec{\Phi}_k \rangle + \frac{1}{V} \int_{A_k} \vec{\Phi}_k \cdot \vec{n}_k dA \tag{2.11}$$

- The volume average of the product of two variables Φ_k and $\vec{u}_k$ may be written as

$$\langle \Phi_k \vec{u}_k \rangle = \epsilon_k \langle \Phi_k \rangle^k \langle \vec{u}_k \rangle^k + \langle \Phi_k'' \vec{u}_k'' \rangle \tag{2.12}$$

where Φ_k'' and $\vec{u}_k''$ are the microscopic deviations of the respective variables, defined as

$$\Phi_k'' = \Phi_k - \langle \Phi_k \rangle^k \tag{2.13}$$

$$\vec{u}_k'' = \vec{u}_k - \langle \vec{u}_k \rangle^k \tag{2.14}$$

The macroscopic transport equation is found by taking the volume average of Equation (2.1), and when combined with the above theorems results in the following:

$$\begin{aligned} \frac{\partial \langle \Phi_k \rangle}{\partial t} + \nabla \cdot \frac{1}{\epsilon_k} \langle \Phi_k \rangle \langle \vec{u}_k \rangle &= \nabla \cdot \langle \vec{J}_k \rangle + \langle \boldsymbol{S}_k \rangle + \frac{1}{V} \int_{A_k} \Phi_k \left(\vec{w}_k - \vec{u}_k \right) \cdot \vec{n}_k dA \\ &+ \frac{1}{V} \int_{A_k} \vec{J}_k \cdot \vec{n}_k dA - \nabla \cdot \langle \Phi_k'' \vec{u}_k'' \rangle \end{aligned} \tag{2.15}$$

Hence, the volume averaging process produces two extra terms related to interfacial effects (third and fourth terms on right hand side of Equation (2.15)), and one extra term related to the microscopic deviation of $\langle \Phi_k \rangle$ (fifth term on right hand side of Equation (2.15)). The treatment of these terms for the respective transport quantity is presented next. For each transport quantity, the following assumptions are considered: fluid and solid phases are incompressible; volume fractions ϵ_f and ϵ_s are constant spatially; the fluid-solid interface is a no-slip, no-penetration surface; the flow is steady; and body forces are negligible. In addition, because the microscopic flow is considered laminar, the macroscopic flow is also assumed to be laminar. Modeling of turbulent flows in porous media is greatly complicated by the existence of source terms created by the combination of volume averaging and ensemble averaging, and is beyond the scope of the present study. The reader is referred to recent works in the literature [28, 36, 37, 59, 60, 69] for more details on this subject.

2.2.1 Macroscopic Conservation of Mass

For the conservation of mass, $\Phi_k = \rho_k$, $\vec{J}_k = 0$, and $\boldsymbol{S}_k = 0$. Substituting these quantities for the fluid into Equation (2.15) results in

$$\frac{\partial \langle \rho_f \rangle}{\partial t} + \nabla \cdot \frac{1}{\epsilon_f} \langle \rho_f \rangle \langle \vec{u}_f \rangle = \frac{1}{V} \int_{A_f} \rho_k \left(\vec{w}_f - \vec{u}_f \right) \cdot \vec{n}_f dA - \nabla \cdot \langle \rho_k'' \vec{u}_k'' \rangle \tag{2.16}$$

Some simplifications can be made based upon the assumptions stated above. Since the flow is steady, the temporal term is zero. In addition, both $\vec{w}_f$ and $\vec{u}_f$ are zero at the interface, so the interfacial term drops out. Because the fluid is incompressible, the density of the fluid is constant within V_f, so that the microscopic deviation term is eliminated. Hence, the final form of the macroscopic conservation of mass equation for the fluid is simply

$$\nabla \cdot \langle \vec{u}_f \rangle = 0 \tag{2.17}$$

The conservation of mass does not need to be considered for the solid due to the assumptions taken.

2.2.2 Macroscopic Conservation of Momentum

Since the solid is stationary, only the fluid momentum needs to be considered. For the fluid, $\Phi_f = \rho_f \vec{u}_f$, $\vec{J}_f = -p_f \boldsymbol{I} + \mu_f \left[\nabla \vec{u}_f + (\nabla \vec{u}_f)^t\right]$ since the fluid is Newtonian ($\boldsymbol{I}$ denotes the identity matrix and superscript t the transpose), and $\boldsymbol{S}_f = 0$ since body forces have been neglected. Substitution of these quantities into Equation (2.15) yields:

$$\begin{aligned}\frac{\partial \langle \rho_f \vec{u}_f \rangle}{\partial t} + \nabla \cdot \frac{1}{\epsilon_f} \langle \rho_f \vec{u}_f \rangle \langle \vec{u}_f \rangle &= -\nabla \langle p_f \rangle + \nabla \cdot \left\langle \mu_f \left[\nabla \vec{u}_f + (\nabla \vec{u}_f)^t\right] \right\rangle \\ &+ \frac{1}{V} \int_{A_f} \left(-p_f \boldsymbol{I} + \mu_f \left[\nabla \vec{u}_f + (\nabla \vec{u}_f)^t\right]\right) \cdot \vec{n}_f dA \\ &- \nabla \cdot \langle (\rho_f \vec{u}_f)'' \vec{u}_f'' \rangle \end{aligned} \tag{2.18}$$

After application of the above assumptions, the macroscopic momentum equation reduces to the following form:

$$\frac{\rho_f}{\epsilon_f^2} \langle \vec{u}_f \rangle \cdot \nabla \langle \vec{u}_f \rangle = -\nabla \langle p_f \rangle^f + \frac{\mu_f}{\epsilon_f} \nabla^2 \langle \vec{u}_f \rangle - \boldsymbol{M}_f \tag{2.19}$$

where the contributions from the interfacial resistance and microscopic deviation are combined into the interfacial momentum source term, $\boldsymbol{M}_f$.

2.2.3 Macroscopic Conservation of Energy

In the study of porous media flows, the assumption of local thermodynamic equilibrium (LTE) is often employed to simplify the analysis. Since the LTE assumption presumes that all phases are isothermal within the REV, only one energy equation needs to be solved. In some applications, such as nuclear systems [2, 62], the LTE assumption must be relaxed due to the combination of high porosity and significant internal heat generation, radiation, or transient effects. As illustrated in the previous chapter, the fiber array application may show significant departure from

LTE, hence this assumption is not taken for the present study. As a result, energy equations for both fluid and solid phases must be considered.

For the fluid phase, $\Phi_f = \rho_f c_{p,f} T_f$ under the assumption of constant specific heats; $\vec{J}_f = \boldsymbol{k}_f \nabla T_f$, where $\boldsymbol{k}_f$ is the fluid thermal conductivity tensor; and $\boldsymbol{S}_f = 0$. (Radiation has not been included since the fluid is transparent.) Substituting the above into the general macroscopic transport equation yields the following:

$$\begin{aligned} \frac{\partial \langle \rho_f c_{p,f} T_f \rangle}{\partial t} + \nabla \cdot \frac{1}{\epsilon_f} \langle \rho_f c_{p,f} T_f \rangle \langle \vec{u}_f \rangle &= \nabla \cdot \langle \boldsymbol{k}_f \nabla T_f \rangle - \frac{1}{V} \int_{A_f} (\boldsymbol{k}_f \nabla T_f) \cdot \vec{n}_f dA \\ &\quad - \nabla \cdot \langle (\rho_f c_{p,f} T_f)'' u_f'' \rangle \end{aligned} \tag{2.20}$$

This equation can be reduced to

$$\rho_f c_{p,f} \nabla \cdot \langle T_f \rangle^f \langle \vec{u}_f \rangle = \nabla \cdot \langle \boldsymbol{k}_f \nabla T_f \rangle + E_f \tag{2.21}$$

where the interfacial and microscopic deviation terms have been grouped into the fluid interfacial energy source term, E_f.

For the solid phase, $\Phi_s = \rho_s c_{p,s} T_s$; $\vec{J}_s = \boldsymbol{k}_s \nabla T_f - \vec{q}_R$, where $\boldsymbol{k}_s$ is the fluid thermal conductivity tensor and $\vec{q}_R$ is radiative heat flux vector; and $\boldsymbol{S}_s = 0$. The conservation of energy for the solid phase is

$$\frac{\partial \langle \rho_s c_{p,s} T_s \rangle}{\partial t} = \nabla \cdot \langle \boldsymbol{k}_s \nabla T_s \rangle - \nabla \cdot \langle \vec{q}_R \rangle - \frac{1}{V} \int_{A_s} (\boldsymbol{k}_s \nabla T_s + \vec{q}_{R,s}) \cdot \vec{n}_s dA \tag{2.22}$$

with the solid velocity vector being taken as zero. If the interfacial terms are included into the solid phase interfacial energy source term, E_s, the resulting equation is

$$0 = \nabla \cdot \langle \boldsymbol{k}_s \nabla T_s \rangle - \langle \nabla \cdot \vec{q}_R \rangle - E_s \tag{2.23}$$

A negative sign appears in front of E_s since the solid phase is presumed to supply energy to the fluid phase. In addition, radiative transfer in the medium and at the interface is accounted for in the term $\langle \nabla \cdot \vec{q}_R \rangle$.

2.2.4 Macroscopic Radiative Transport

Figure 2.1 illustrates the general aspects of radiative exchange in a participating medium. Incident radiation may be scattered out of the control volume, or may be

absorbed by the medium. The net outflow of radiation is also augmented by emission if the medium is not at absolute zero temperature. Radiative transfer is a complex phenomena, as it depends upon the intensity and wavelength, λ, of the incident radiation, the spectral radiative properties of the medium, and the temperature. In mathematical terms, the change along length ds of the incident radiative heat flux due to scattering, $(dI_\lambda)_s$, is written as follows [39, 51]:

$$(dI_\lambda)_s(\vec{s}) = ds\frac{\sigma_\lambda}{4\pi}\int_{4\pi} I_\lambda(\vec{s}_i)\Phi_\lambda(\vec{s},\vec{s}_i)d\Omega_i \tag{2.24}$$

The amount of scattering is controlled by the spectral scattering coefficient, σ_λ, and by the spectral scattering phase function, $\Phi_\lambda(\vec{s},\vec{s}_i)$. Since $\Phi_\lambda(\vec{s},\vec{s}_i)$ is a function of the angle between the incident radiative flux, $\vec{s}_i$, and the outgoing flux, $\vec{s}$, the net scattering must be integrated over all solid angles. Attenuation of radiation due to absorption is expressed as [39, 51]

$$(dI_\lambda)_a = -\kappa_\lambda I_\lambda ds \tag{2.25}$$

where κ_λ is the spectral absorption coefficient. Emission is related to absorption in that coefficients for emission and absorption must be the same to maintain thermodynamic equilibrium [39, 51]; hence,

$$(dI_\lambda)_e = \kappa_\lambda I_{b\lambda} ds \tag{2.26}$$

where $I_{b\lambda}$ is the spectral blackbody intensity evaluated at the medium temperature.

Radiation heat transfer has been investigated in a number of porous media applications, as reviewed by Kaviany and Singh [33] and Tien and Vafai [57]. The contribution of radiation heat transfer is accounted for in the macroscopic energy equation by the divergence of the radiative heat flux, $\langle\nabla\cdot\vec{q}_R\rangle$, which is defined as follows [33, 39, 51, 57]:

$$\langle\nabla\cdot\vec{q}_R\rangle = \int_0^\infty \kappa_\lambda\left(4\pi I_{b\lambda} - \int_{4\pi} I_\lambda d\Omega\right)d\lambda \tag{2.27}$$

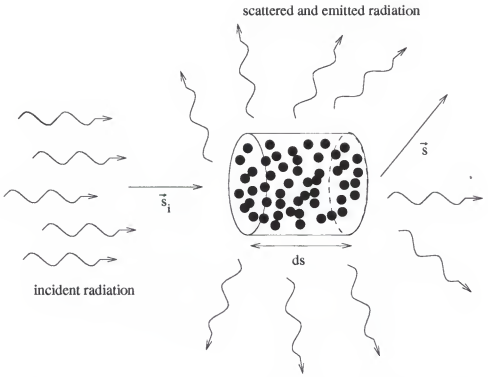

Figure 2.1: Schematic of radiative transfer in a participating medium.

(The functional dependency of I_λ on $\vec{s}$ and $\vec{s}_i$ has been dropped for convenience.) Combining the attenuation and augmentation of radiation as described previously yields the radiative transfer equation (RTE) [39, 51]:

$$\vec{s} \cdot \nabla I_\lambda = \kappa_\lambda I_{b\lambda} - \beta_\lambda I_\lambda + \frac{\sigma_\lambda}{4\pi} \int_{4\pi} I_\lambda \Phi_\lambda d\Omega \tag{2.28}$$

where β_λ is the extinction coefficient ($\beta_\lambda = \kappa_\lambda + \sigma_\lambda$). Because the fluid is nonparticipating, the spectral blackbody intensity is computed based upon the local solid temperature, $\langle T_s \rangle^s$, as shown below [39, 51]:

$$I_{b\lambda} = \frac{2 h_P c_o^2}{n^2 \lambda^5 (\exp(h_P c_o / n \lambda k_B \langle T_s \rangle^s) - 1)} \tag{2.29}$$

where c_o is the speed of light in vacuum, h_P is Planck's constant, n is the refractive index, and k_B is Boltzmann's constant.

Evaluation of $\langle \nabla \cdot \vec{q}_R \rangle$ and the RTE requires knowledge of the spectral absorption and scattering coefficients, along with the spectral scattering phase function. Most porous media can be treated as a collection of particles, and as such the radiative

properties are dependent upon three parameters [39, 51]: the real and imaginary indices of refraction, n and k; the size parameter, $x_R = \pi d_p/\lambda$, where d_p is the characteristic particle size; and the clearance-to-wavelength ratio, c/λ, where c is the characteristic interparticle separation distance. For this study, it is presumed that $c/\lambda \gg 1$, hence the assumption of independent scattering is valid. Absorption and scattering caused by each particle may be written by absorption and scattering efficiencies, Q_a and Q_s [39, 51]:

$$Q_a = \frac{4C_a}{\pi d_p^2} \tag{2.30}$$

and

$$Q_s = \frac{4C_s}{\pi d_p^2} \tag{2.31}$$

The absorption and scattering cross sections, C_a and C_s, are functions of the refractive indices and the size parameter. Solutions to C_a and C_s, along with the spectral scattering phase function, can be found by solving the Maxwell equations for the given particle, with the Mie scattering theory being one of the more utilized methods. As the Maxwell equations are rather complex, the reader is referred to the literature for their formulations [9, 64]. Finally, the spectral absorption and scattering coefficients are found by summing up the contributions from each particle in the aggregate [39, 51]:

$$\kappa_\lambda = NC_a \tag{2.32}$$

and

$$\sigma_\lambda = NC_s \tag{2.33}$$

where N is the number of particles per unit volume. The values of κ_λ, σ_λ, and Φ_λ for the specified fiber array insert are presented in a later chapter.

2.3 Treatment of Macroscopic Source Terms

The primary difficulty encountered in applying the macroscopic equations to a given problem is the specification of the additional source terms arising from

the volume averaging operation. This is directly analogous to the closure problem encountered in the analysis of turbulent flows [6, 49]. These terms are now examined in more detail (a discussion of radiative issues is given in a subsequent chapter).

2.3.1 Momentum Source Term

Considering uni-directional flows in porous media with negligible convection and diffusion, the pressure gradient $-\nabla\langle p_f\rangle^f$ can be computed via the well-known Darcy law [4, 6],

$$-\nabla\langle p_f\rangle^f = \frac{\mu_f\langle v_f\rangle}{K} \tag{2.34}$$

for cases where the streamwise volume averaged fluid velocity, $\langle v_f\rangle$, is small. As previously mentioned, K is the intrinsic or Darcian permeability in the streamwise direction, with the value of $\sqrt{K}$ characteristic of the microstructure pore size [6]. Upon inspection of the macroscopic momentum equation, Equation (2.19), the volume averaged pressure gradient is balanced by the momentum source term if the macroscopic velocity field is periodic. Hence, each component of $\boldsymbol{M}_f$ can be represented by Darcy's law for small velocities; for instance,

$$M_{fx} = \frac{\mu_f\langle u_f\rangle}{K_x} \tag{2.35}$$

in the x coordinate direction. It can be seen from this equation that the permeability is a tensor quantity, so anisotropic effects are accounted for (off-diagonal terms are usually not included in porous media flows [3, 4]). Non-Darcy effects become important when the Darcian Reynolds number, $Re_{\sqrt{K}}$, is greater than one [6]:

$$Re_{\sqrt{K}} = \frac{\rho_f v_f\sqrt{K}}{\mu_f} \tag{2.36}$$

In this instance, $-\nabla\langle p_f\rangle^f$ (or each component of $\boldsymbol{M}_f$) can be determined either by the Ergun equation [21]:

$$-\nabla\langle p_f\rangle^f = A\frac{{\epsilon_f}^2}{(1-\epsilon_f)^3}\frac{\mu\langle v_f\rangle}{{d_p}^2} + B\frac{\epsilon_f}{(1-\epsilon_f)^3}\frac{\rho\langle v_f\rangle^2}{d_p} \tag{2.37}$$

or by the Forchheimer equation [2, 4, 6],

$$-\nabla\langle p_f\rangle^f = \frac{\mu\langle v_f\rangle}{K} + \frac{F\rho}{\sqrt{K}}\langle v_f\rangle^2 \tag{2.38}$$

In these equations, A and B are the first and second Ergun coefficients, d_p is the characteristic particle diameter, and F is the Forchheimer term. Although these two expressions have a slightly different form, each employs one term to handle low velocity situations (creeping flow) and a second term to include the effects of turbulence and/or inertia (hence the appearance of velocity squared). As both of these equations are empirical in nature, there is no guarantee as to their validity for a specified porous media. Later, the validity of Equations (2.37) and (2.38) will be investigated for cylinder arrays via microscopic modeling.

2.3.2 Energy Source Term

At the interface between fluid and solid phases, the application of Newton's law of cooling may be applied to determine the heat transfer rate, q:

$$q = h_{fs}(T_{fs} - T_r) \tag{2.39}$$

where h_{fs} is the interfacial heat transfer coefficient, T_{fs} is the interfacial temperature and T_r is the reference temperature. In order to develop a more general form of the interfacial energy source term, a number of assumptions are required. First, it is assumed that the solid phase has a relatively high conductivity, so that microscopic deviations of T_s are negligible from a large-scale viewpoint; hence, $T_{fs} = \langle T_s\rangle^s$. In addition, $\langle T_f\rangle^f$ is taken as the reference temperature. Thus, the microscopic energy balance over the REV with specific interfacial surface area a_{fs} yields [2]

$$E_f = -E_s = h_{fs}a_{fs}\left(\langle T_s\rangle^s - \langle T_f\rangle^f\right) \tag{2.40}$$

As with the momentum source term tensor, the value of h_{fs} will be investigated in a subsequent chapter.

Although not a source term of the macroscopic energy equation, the conduction term is now given further attention. In order to simplify treatment of the conduction term, an effective conductivity is presumed [52, 67]; thus, for the fluid phase,

$$\nabla \cdot \langle \boldsymbol{k}_f \nabla T_f \rangle = \boldsymbol{k}_{ef} \epsilon_f \nabla^2 \langle T_f \rangle^f \tag{2.41}$$

where $\boldsymbol{k}_{ef}$ is the effective fluid conductivity tensor. A similar equation may be written for the solid phase by replacing f with s. The intrinsic volume averaged temperature is considered in order to be consistent with the other macroscopic energy equation terms.

2.4 Summary of Macroscopic Governing Equations

If non-equilibrium local thermodynamics and radiative transfer are important, the following macroscopic equations are to be solved for unknowns $\langle \vec{u}_f \rangle$, $\langle p_f \rangle^f$, $\langle T_f \rangle^f$, $\langle T_s \rangle^s$, $\langle \nabla \cdot \vec{q}_R \rangle$, and I_λ (six equations with six unknowns):

Conservation of mass (fluid):

$$\nabla \cdot \langle \vec{u}_f \rangle = 0 \tag{2.42}$$

Conservation of momentum (fluid):

$$\frac{\rho_f}{\epsilon_f^2} \langle \vec{u}_f \rangle \cdot \nabla \langle \vec{u}_f \rangle = -\nabla \langle p_f \rangle^f + \frac{\mu_f}{\epsilon_f} \nabla^2 \langle \vec{u}_f \rangle - \boldsymbol{M}_f \tag{2.43}$$

Conservation of energy (fluid):

$$\rho_f c_{p,f} \nabla \cdot \langle T_f \rangle^f \langle \vec{u}_f \rangle = \boldsymbol{k}_{ef} \epsilon_f \nabla^2 \langle T_f \rangle^f + h_{fs} a_{fs} \left(\langle T_s \rangle^s - \langle T_f \rangle^f \right) \tag{2.44}$$

Conservation of energy (solid):

$$0 = \boldsymbol{k}_{es} \epsilon_s \nabla^2 \langle T_s \rangle^s - h_{fs} a_{fs} \left(\langle T_s \rangle^s - \langle T_f \rangle^f \right) - \langle \nabla \cdot \vec{q}_R \rangle \tag{2.45}$$

Divergence of radiative heat flux:

$$\langle \nabla \cdot \vec{q}_R \rangle = \int_0^\infty \kappa_\lambda \left(4\pi I_{b\lambda} - \int_{4\pi} I_\lambda d\Omega \right) d\lambda \tag{2.46}$$

Radiative transfer equation:

$$\vec{s} \cdot \nabla I_\lambda = \kappa_\lambda I_{b\lambda} - \beta_\lambda I_\lambda + \frac{\sigma_\lambda}{4\pi} \int_{4\pi} I_\lambda \Phi_\lambda d\Omega \tag{2.47}$$

The remaining task is to evaluate the various macroscopic source terms and coefficients for the fiber array application. A microscopic study aimed at determining the forms of $\boldsymbol{M}_f$ and h_{fs} for cylinder arrays is presented in next chapter, while the effective conductivities and radiative properties are addressed subsequently.

2.5 Multiscale Modeling Approach

At this stage the specification of the macroscopic momentum and energy source term coefficients is incomplete, since values for permeability, the non-Darcy coefficients, and the interfacial convective heat transfer coefficient have not been established. In the past, these coefficients have been determined by flow experiments, where the global pressure drop across a porous media is correlated to the flow rate by least squares curve fitting [4, 6]. More recently, numerical analyses have been used to determine these coefficients [65]. The determination of the macroscopic source terms depends upon the approach used in modeling flow phenomena at microscopic and macroscopic levels. Generally speaking, the multiscale modeling approach can be classified into the following categories: coupled modeling, where iteration occurs between computations at microscopic and macroscopic levels; and uncoupled modeling, where multiscale computations are performed independently. The investigation of Shyy and Vu [50] serves as an excellent example of a coupled modeling procedure. In this study, the flow through a complex array of vanes inside a hydraulic turbine is modeled as porous media. Results from the macroscopic computations supply boundary conditions to microscopic analyses, which then provide information regarding the effective macroscopic flow resistance. The main drawback of a coupled modeling approach is that the overall computational effort may be very intensive,

requiring a large amount of macroscopic-level/microscopic-level iterations and CPU time.

Regarding flows in fiber array inserts, the complexity of interfacial transfer may be effectively and efficiently handled by an uncoupled modeling approach. This method is readily employed in this instance since a range of boundary conditions for microscopic flow calculations can be established beforehand. The essential steps that are taken for the multiscale analyses featured in the current investigation are as follows:

1. *Analyze the microscopic flow field.* This may be accomplished by numerically solving the Navier-Stokes equations within the REV by finite element, finite difference, or control volume techniques. Lattice-gas methods have also been explored for use in microscopic analyses [65].

2. *Compute the volume average of the flow field variables within the REV.* Once the microscopic flow field is known, the numerical integration of the flow field variables within the REV is straightforward.

3. *Evaluate the macroscopic coefficients as a function of the porous media properties and the flow conditions.* In other words, coefficients must be correlated to the particular conditions that are in question. In some cases, it may be necessary to perform a large number of analyses in order to construct the database for correlating purposes. However, no additional microscopic computations need to be performed once the correlations are established.

4. *Conduct the specific macroscopic analysis.*

2.6 Numerical Modeling Considerations

To numerically solve the microscopic governing equations, Equations (2.2) – (2.4), or the macroscopic governing equations, Equations (2.42) – (2.47), a control

volume procedure is adopted in this investigation. The SIMPLE algorithm (Semi-Implicit Method for Pressure-Linked Equations) as presented by Patankar [44] is employed for macroscopic continuity, momentum, and energy equations. Extensions to the SIMPLE algorithm are made to handle curvilinear coordinates [48, 55] and are utilized in the microscopic computations. Solution to the RTE is handled by the control volume procedure developed by Chai [10], which shares many similarities to the SIMPLE algorithm. The general concepts featured in these algorithms are described below for two-dimensional flows. Specific issues related to the particular application are addressed in later chapters.

2.6.1 SIMPLE Algorithm and Extension to Curvilinear Coordinates

The SIMPLE algorithm is a pressure-correction procedure, whereby the velocity field as computed by the linearized momentum equations is corrected by the continuity equation; iteration continues until all equations are satisfied. Figure 2.2 illustrates a typical control volume within the computational domain for a two-dimensional cartesian grid. For convenience, a staggered grid is employed, with the velocity components u and v offset from the center of the control volume where pressure p is applied. After integrating the momentum equation in each direction over the control volume at grid location (i, j) with size $\Delta x \Delta y \cdot 1$, the linearized form of the momentum equations appears below:

$$a_w u(i,j) = \sum(a_{nb} u^*_{nb}) + b + (p^*(i-1,j) - p^*(i,j))A_w \tag{2.48}$$

$$a_s v(i,j) = \sum(a_{nb} v^*_{nb}) + b + (p^*(i,j-1) - p^*(i,j))A_s \tag{2.49}$$

In these expressions, superscript $*$ refers to the previous values of velocity and pressure, subscript nb refers to neighboring values, and A refers to the area of the control volume interface at west, w, and south, s, sides. Variable b is the momentum source term, which is zero for microscopic flows; in macroscopic flows, b accounts for the added resistance of the porous media. Contributions of convection and diffusion

are incorporated into the a coefficients, as exemplified below for a_w:

$$a_w = D_w A(|P_w|) + [[F_w, 0]] \tag{2.50}$$

where the diffusion term, D_w, is defined as

$$D_w = \frac{\mu_f \Delta y}{\delta x_w} \tag{2.51}$$

and the convection term, F_w, is defined as

$$F_w = (\rho_f u(i,j))\Delta y \tag{2.52}$$

In Equation (2.50), function A depends upon the particular differencing scheme and is a function of the Peclet number, $P_w = F_w/D_w$. For example, A takes on the following form for central differencing:

$$A(|P_w|) = 1 - 0.5|P_w| \tag{2.53}$$

Double brackets [[ ]] signify that the maximum positive value of the two quantities is to be considered.

After the velocity field is computed, the pressure is determined via the pressure correction equations. The value of the pressure at each control volume is decomposed as follows:

$$p(i,j) = p^*(i,j) + p'(i,j) \tag{2.54}$$

where $p'(i,j)$ is the pressure correction, which approaches zero as the solution converges. The pressure correction equation is derived from the continuity equation and may be expressed as follows:

$$a_P p'(i,j) = a_E p'(i+1,j) + a_W p'(i-1,j) + a_S p'(i,j-1) + a_N p'(i,j+1) + b \tag{2.55}$$

where

$$a_{E,W} = (\rho_f d)_{e,w} \Delta y \tag{2.56}$$

$$a_{S,N} = (\rho_f d)_{s,n} \Delta x \tag{2.57}$$

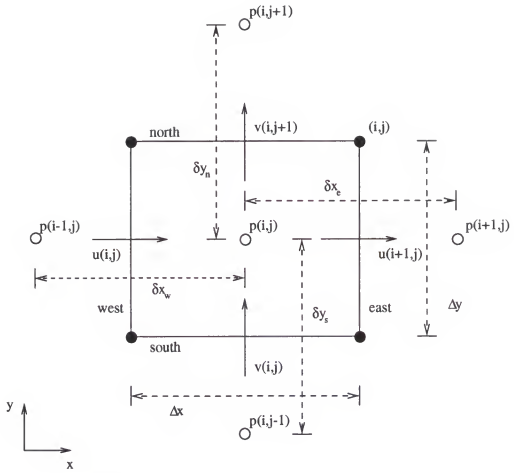

Figure 2.2: Schematic of typical control volume.

$$d_{e,w,s,n} = \left(\frac{A}{a}\right)_{e,w,s,n} \tag{2.58}$$

$$a_P = a_E + a_W + a_S + a_N \tag{2.59}$$

$$b = [(\rho_f u^*(i,j)) - (\rho_f u^*(i+1,j))]\Delta y + [(\rho_f v^*(i,j)) - (\rho_f v^*(i,j+1))]\Delta x \tag{2.60}$$

After the p' field is determined from Equation (2.55), the p field is corrected by the pressure correction equation. Velocity components are also corrected in a similar manner:

$$u(i,j) = u^*(i,j) + u'(i,j)\ ,\ v(i,j) = v^*(i,j) + v'(i,j) \tag{2.61}$$

The velocity corrections are calculated from

$$a_w u'(i,j) = \sum(a_{nb} u'_{nb}) + (p'(i-1,j) - p'(i,j))A_w \tag{2.62}$$

with similar formulations appearing for the other velocity components. With the velocity field known, the linearized momentum equations are again solved, and the process continues until convergence is achieved.

In this investigation, momentum and energy equations are not coupled to one another, hence the energy equation may be solved for an already known velocity and pressure field. With the staggered grid, temperature $T(i,j)$ is taken to be located at the center of control volume (i,j). The linearized form of the energy equation appears below:

$$a_P T(i,j) = a_E T(i+1,j) + a_W T(i-1,j) + a_N T(i,j+1) + a_S T(i,j-1) + b \tag{2.63}$$

In this expression, the a coefficients take on the same form as in the momentum equations, except that the diffusion term is written as

$$D_w = \frac{k_f \Delta y}{\delta x_w} \tag{2.64}$$

Source term b in the above accounts for interfacial convective heat transfer and also radiative contributions.

The above procedure forms a general basis for analysis in curvilinear coordinates, but certain modifications need to be made to handle this situation. As described

in Shyy [48] and Thakur et al. [55], the curvilinear modeling approach employs combined cartesian-contravariant velocity components to enforce the conservation laws consistently. In more specific terms, the pressure correction equation is altered to meet this requirement, and hence has a different form than Equation (2.55). Also, care is taken to ensure that mass conservation holds when converting between cartesian and contravariant velocity components. As in the SIMPLE algorithm, the velocity, pressure correction, and temperature equations are solved sequentially, and include appropriate discretization schemes and boundary conditions. The reader may consult Shyy [48] and Thakur et al. [55] for the detailed aspects of this procedure.

2.6.2 Solution to the RTE

The solution procedure for the RTE shares the same spatial grid as above, but also requires angular discretization to account for radiation in all directions. As shown in Figure 2.3(a), the direction of radiative intensity is described by vector $\vec{s}$. Polar angle θ and azimuthal angle ϕ are used to specify $\vec{s}$ in the following manner:

$$\vec{s} = \sin\theta\cos\phi\ \vec{e}_x + \sin\theta\sin\phi\ \vec{e}_y + \cos\theta\ \vec{e}_z \tag{2.65}$$

where $\vec{e}_x$, $\vec{e}_y$, and $\vec{e}_y$ are the unit direction vectors in cartesian coordinates. Figure 2.3(b) shows solid angle $\Delta\Omega$ resulting from the discretization of the θ and ϕ domains, where

$$\Delta\Omega = \int_{\Delta\phi}\int_{\Delta\theta} \sin\theta d\theta d\phi \tag{2.66}$$

For a given direction $\vec{s}$, the control volume form of the RTE is as follows (refer to Figure 2.3(c), and note that spectral dependency is not assumed for clarity):

$$(I_e - I_w)(\Delta y)D_{cx} + (I_n - I_s)(\Delta x)D_{cy} = (-\beta_m I(i,j) + S_m)\,\Delta x\Delta y\Delta\Omega \tag{2.67}$$

The terms D_{cx} and D_{cy} are the direction cosines, which are defined as

$$D_{cx,cy} = \int_{\Delta\Omega} (\vec{s}\cdot\vec{n}_{x,y})d\Omega \tag{2.68}$$

where $\vec{n}$ is the unit normal vector in direction x or y. Since the RTE is linearized, the modified extinction coefficient, β_m, and the modified source term, S_m, are expressed as follows:

$$\beta_m = \beta - \frac{\sigma}{4\pi}\Phi(\vec{s},\vec{s})\Delta\Omega \tag{2.69}$$

and

$$S_m = \kappa I_b(i,j) + \frac{\sigma}{4\pi}\sum_{\vec{s}\neq\vec{s}_i} I(i,j)\Phi(\vec{s},\vec{s}_i)\Delta\Omega \tag{2.70}$$

Finally, the intensities at the boundaries are related to nodal intensities via the step scheme. Inflow intensities, which are present at west and south boundaries in Figure 2.3(c), are presumed to take on the values of their upstream neighbors: $I_w = I(i-1,j)$ and $I_s = I(i,j-1)$. The remaining boundaries feature outflow of radiation, and these intensities are approximated by the intensity at the current control volume: $I_e = I_n = I(i,j)$.

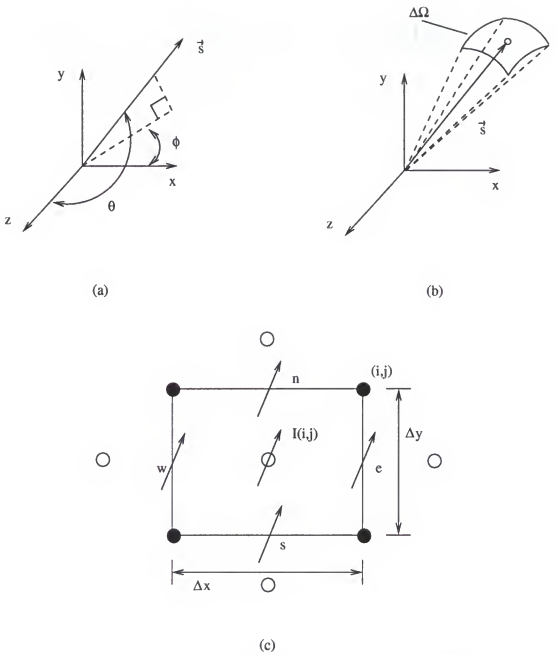

Figure 2.3: General features of radiative transfer modeling – (a) direction vector $\vec{s}$; (b) angular control volume $\Delta\Omega$; (c) spatial control volume.

CHAPTER 3
MICROSCALE MODELING OF FLUID FLOW AND HEAT TRANSFER IN SPARSE, PERIODIC CYLINDER ARRAYS

As stated in the previous chapter, the macroscopic governing equations for flows in porous media feature source terms which are unknown *a priori*; experimental or numerical studies must be performed to determine these values for a particular application. In this chapter, a microscopic analysis of fluid flow and heat transfer in cylinder arrays is presented. The term 'cylinder' has been used to describe the array rather than 'fiber' in order to maintain generality. Flow of fluids through cylinder arrays is important in other applications besides the problem considered herein, and include filtration, biological systems, and heat exchangers. Both square and triangular arrays are considered, with fluid volume fractions ranging from 0.80 to 0.99.

A crucial simplifying assumption taken for the microscopic analysis is that the flow and heat transfer are fully developed. Since the arrangement of the cylinder arrays is periodic, the flow field itself is periodic when the fully developed assumption is taken. If the flow is aligned longitudinally to the cylinder array, entrance effects are negligible for cases where the cylinder length greatly exceeds the cylinder diameter, d. For flows transverse to the cylinder array, the influence of entrance effects decays for a cylinder array with a large number of rows (roughly greater than 20 [71]). In other words, for this investigation the cylinders are taken to be infinitely long, and the size of the array itself is infinite. Hence, only a solitary cylinder within the array, or a portion of a single cylinder with symmetry conditions employed, needs to be considered for the microscopic analysis.

3.1 Longitudinal Flow

Figure 3.1 shows square and triangular arrays of cylinders with diameter d and spacing c, and the flow is oriented parallel to the cylinder axis (z coordinate direction). The cylinder spacing is fixed by specification of the fluid volume fraction or porosity, ϵ_f, where

$$\epsilon_f = 1 - \frac{\pi}{4}\left(\frac{c}{d}\right)^{-2} \tag{3.1}$$

for the square array, and

$$\epsilon_f = 1 - \frac{\pi}{2\sqrt{3}}\left(\frac{c}{d}\right)^{-2} \tag{3.2}$$

for the triangular array. The range of porosities considered, $0.80 \leq \epsilon_f \leq 0.99$, results in a sparsely spaced array, with c/d ranging from about two to over ten. Since laminar flow is assumed, the absence of an adverse pressure gradient keeps the flow attached, thus inertial effects are not present here. Solutions to the microscopic flow equations under these conditions are available in the literature. Åström et al. [3] have reviewed a number of investigations of Darcian flow through aligned fiber beds, and report the functional form of the longitudinal permeability K_z as

$$\frac{K_z}{C_z} = \frac{d^2}{16\epsilon_s} \tag{3.3}$$

The parameter C_z has been obtained by Drummond and Tahir [16] from microscopic Stokes flow analyses. Closed-form solutions for square and triangular arrays, respectively, appear below [16]:

$$C_z = \ln\left(\frac{1}{\epsilon_s}\right) - 1.476 + 2\epsilon_s - 0.5{\epsilon_s}^2 - \frac{0.05097{\epsilon_s}^4}{1 + 1.52{\epsilon_s}^2} \tag{3.4}$$

and

$$C_z = \ln\left(\frac{1}{\epsilon_s}\right) - 1.498 + 2\epsilon_s - 0.5{\epsilon_s}^2 - 0.002514\epsilon_s^6 \tag{3.5}$$

Values for K_z, normalized by d^2, are shown in Figure 3.2 as a function of fluid porosity for square and triangular arrays. The longitudinal permeabilities for the

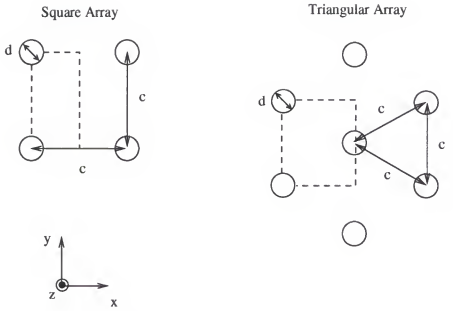

Figure 3.1: Schematic of square and triangular arrays.

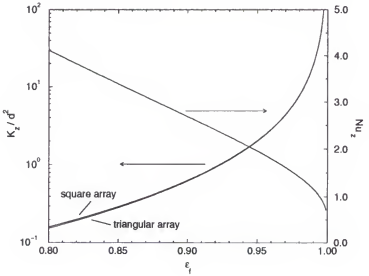

Figure 3.2: Longitudinal permeability and Nusselt number versus fluid volume fraction for square and triangular arrays.

two arrays are nearly indistinguishable, since the spacing-to-diameter ratios are large for the porosities considered.

With regards to heat transfer, Sparrow et al. [54] studied heat transfer in triangular arrays and presented the Nusselt number for longitudinal flow over a broad range of c/d. The authors determined that the Nusselt number could be accurately predicted with an equivalent annulus formulation, provided that c/d was greater than 1.5. In this simplification, the flow area for the array in question is equated to the case of flow in an annular section. The inner surface supplies heat to the fluid, while the outer surface is adiabatic, and circumferential variations in the temperature field are ignored. Figure 3.2 shows the Nusselt number Nu_z resulting from the equivalent annulus formulation, with

$$Nu_z = \frac{hd}{k_f} \tag{3.6}$$

Because square and triangular arrays have identical flow areas, Nu_z is the same for each array for a given porosity. Also, as the porosity approaches one (i.e., a solitary cylinder surrounded by an infinite fluid), Nu_z asymptotically approaches zero.

3.2 Transverse Flow

Transverse or cross flow in periodic cylinder arrays has been the focus of a large number of investigations; review articles by Åström et al. [3] and Žukauskas [70, 71] list over 300 references related to flows in fibrous media and tube bundles, respectively. Despite this wealth of information, questions remain concerning the quantitative nature of flow in high porosity cylinder arrays: treating the cylinder array as a porous media, can flow be considered Darcian and, if not, can other simplifying procedures be used to approximate the flow stream. For the case of flows in sparse, periodic arrays, where the spacing to diameter ratio c/d is greater than two, previous studies have investigated creeping flow conditions alone, such as Clague and Phillips [14], Drummond and Tahir [16], and Sangani and Acrivos [46].

Nusselt number correlations are available for flows within tube bundles [70, 71, 72], but there is little data for flows in sparse arrays.

This section presents an investigation into laminar fluid flow and heat transfer transverse to square and triangular periodic arrays of cylinders with large spacing ratios. As before, fluid volume fractions ϵ_f range from 0.80 to 0.99, while particle Reynolds numbers Re_d (where d is the cylinder diameter) vary from approximately 3 to 160. The macroscopic effects of the cylinder arrays are assessed by considering the arrays as a porous media, with coefficients appearing in the macroscopic equations determined by volume averaging of the microscopic flow field variables. Non-Darcian behavior is expected to play an important role due to the combination of large fluid volume fraction and high Reynolds number. Comparisons are made to the Ergun and Forchheimer relations to examine their validity in this porosity range. For the case of heat transfer, LTE is not assumed, and both constant wall temperature and constant wall heat flux conditions are investigated.

3.2.1 Problem Description and Numerical Approach

Referring to Figure 3.1, the flow is taken to be oriented in the y coordinate direction for transverse flow. (Other flow directions are possible, of course, but the present analysis is limited to only a single transverse direction.) Because the flow is periodic, the problem is reduced to the determination of velocity, pressure, and temperature fields in the fluid surrounding a solitary cylinder within the array. These flow domains are shown in Figure 3.1 with dashed lines, which are taken to be the REV for volume averaging purposes (note that symmetry conditions are invoked for the square array). Once the microscopic flow equations are solved, the volume average of the flow variables can be computed, and then the macroscopic terms can be correlated as a function of array type, fluid volume fraction, and flow condition. A finite volume-based numerical procedure, as described by Thakur et al. [55] and Shyy [48], is utilized to solve the microscopic equations, Equations (2.2) – (2.4), in

curvilinear coordinates for two-dimensional flow. This procedure is based on the SIMPLE algorithm [44] extended to curvilinear coordinates and employing mixed cartesian and contravariant velocity components, with a second order upwinding arrangement for convective terms. (A general discussion of the SIMPLE algorithm is included in the previous chapter.)

As illustrated in Figure 3.3, which features a square array with $\epsilon_f = 0.80$, no-slip, no penetration boundary conditions are imposed at the cylinder surface, along with either constant temperature or constant heat flux boundary conditions. The inlet and outlet are periodic, with pressure difference $-\Delta p$ driving the flow. Fluid surfaces not in contact with the cylinder are taken as symmetric and adiabatic. Treatment of the periodic boundary conditions in the context of a finite volume procedure now follows, and is based on concepts presented by Patankar et al. [45].

With regards to the momentum equations, the periodic assumption implies that the velocity components u and v, for two-dimensional flow, must be identical at each streamwise periodic station Y and $Y + c$. Because the flow is pressure driven, the difference in pressure between any two periodic stations must be a constant:

$$p(x, Y) - p(x, Y + c) = -\Delta p \tag{3.7}$$

where $-\Delta p$ is given. Since the SIMPLE algorithm relies on a staggered grid, an overlapping grid scheme is employed for the present analysis, as shown in Figure 3.3. Values for the pressure of the interior cells located just below station Y are determined from Equation (3.7), based on the previous value of the pressure of the cells below downstream station $Y+c$. The pressure of the cells located above station $Y + c$ are found in a similar manner, with the difference being that the upstream station is taken as the known reference.

Temperature specification at the periodic inlet and outlet is dependent upon the wall heating condition. For constant wall heat flux, the difference between

downstream and upstream temperatures is expressed by

$$T(x, Y + c) - T(x, c) = \frac{Q}{\dot{m} c_p} \tag{3.8}$$

where $\dot{m}$ is the mass flow rate, and Q is the total heat rate:

$$Q = \int_{A_s} q_s dA \tag{3.9}$$

where A_s is the total wall surface area and q_s is the wall heat flux. Boundary temperatures are found in a manner directly analogous to the specification of pressure in this instance. The constant wall temperature case requires that two relationships must be satisfied. Because the flow is thermally developed, the difference in temperature between the fluid and the wall exponentially decays to zero, thus the first relation to be met is

$$\frac{T(x, Y) - T_w}{T^*(Y) - T_w} = \frac{T(x, Y + c) - T_w}{T^*(Y + c) - T_w} \tag{3.10}$$

In this expression, $T^*(Y)$ is a reference temperature defined as follows:

$$T^*(Y) = \frac{\int T(x, Y)|V| d\xi}{\int |V| d\xi} \tag{3.11}$$

where V is the contravariant streamwise velocity along the cross flow direction ξ (the reference temperature at $Y + c$ is defined similarly). It should be noted that the reference temperature is identical to the definition of bulk temperature if the absolute value of V is not considered; however, $|V|$ is computed to account for recirculation zones at the inlet or outlet. The second relation which must be met is the following:

$$\frac{d\left(T(x, Y) - T_w\right)/dy}{T^*(Y) - T_w} = \frac{d\left(T(x, Y + c) - T_w\right)/dy}{T^*(Y + c) - T_w} \tag{3.12}$$

First-order differencing is used to handle the derivative of the temperature difference for this relationship. Both Equations (3.10) and (3.12) are used to specify the values inlet and outlet temperatures for the case of constant surface temperature.

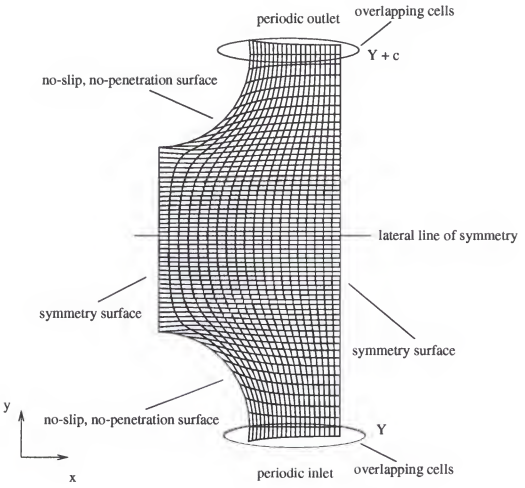

Figure 3.3: Schematic of boundary conditions for cylinder array.

Table 3.1: Grid sensitivity comparison for square array, $\epsilon_f = 0.99$, $-\Delta p = 1.0$ N/m^2.

			$\log_{10}$ normalized residuals:		
Grid Size	Re_d	$\lvert\delta_m\rvert$ (%)	x momentum	y momentum	continuity
21×63	57.9	1.7	-5.3	-4.8	-5.3
41×63	58.3	1.0	-5.4	-4.6	-5.3
21×123	58.8	0.2	-5.0	-4.5	-5.0
41×123	58.9	–	-5.1	-4.2	-5.0

Figure 3.4 illustrates the typical grids used for square and triangular arrays for the extreme ϵ_f values, 0.80 and 0.99. A 21×63 grid is selected for the square array, while a 31×63 grid is chosen for the triangular array, which has a smaller aspect ratio. The grids are constructed to maximize the number of cells adjacent to solid surfaces, where sharp gradients in fluid velocity and temperature are expected. Overlapping grid cells are present at periodic inlet and outlet faces, and care is taken to ensure symmetry about the lateral centerline of the domain. Grid sensitivity was investigated for the square array with $\epsilon_f = 0.99$ under high Reynolds number flow. Table 3.1 shows a comparison of the computed particle Reynolds number resulting from the pressure difference $-\Delta p = 1.0$ N/m^2 for four different grid sizes: 21×63, 41×63, 21×123, and 41×123. Since the maximum relative difference, δ_m, between the finest grid and the coarser grid results is less than 2%, the solution was considered to be grid independent; hence the coarsest grid was selected to minimize computational effort. Normalized residuals are also included in Table 3.1, which are typical values obtained for all other porosities. The solution of the continuity and momentum equations for each array required four to six hours of CPU time on a middle-end workstation (DEC 3000 Model 600), with about 30 minutes for the solution of the energy equation.

Physical properties of the fluid are of air at 300 K [32]: $\rho_f = 1.23$ kg/m^3; $\mu_f = 1.79 \times 10^{-5}$ N-s/m^2; $c_{p,f} = 1006$ J/kg-K; and $k_f = 0.025$ W/m-K [32]. Although

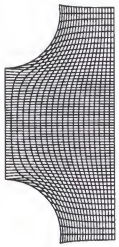

(a)

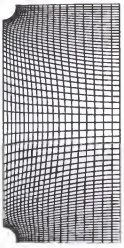

(b)

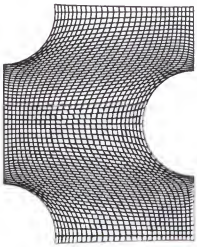

(c)

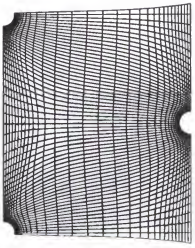

(d)

Figure 3.4: Computational grids for cylinder arrays – (a) square array, $\epsilon_f = 0.80$; (b) square array, $\epsilon_f = 0.99$; (c) triangular array, $\epsilon_f = 0.80$; (d) triangular array, $\epsilon_f = 0.99$.

any other fluid could have been selected, air is chosen to be representative of a gas flow (Prandtl number dependency is not considered in this work).

3.2.2 Results: Fluid Flow

To illustrate the qualitative features of the flow field, streamline plots are shown in Figure 3.5 for the square array and Figure 3.6 for the triangular array under low and high flow rate conditions. For small particle Reynolds numbers, where

$$Re_d = \frac{\rho \langle v_f \rangle d}{\mu} \tag{3.13}$$

a Stokes type of flow field can be seen, with little or no vortex generation behind the cylinders. As Re_d increases, the vortex behind the cylinder grows and extends up to the front of the downstream cylinder where $\epsilon_f = 0.80$. Presentation of the quantitative flow features now follows by treating Darcian and non-Darcian flow regimes individually.

As stated before, Darcy flow is valid for cases where the Darcian Reynolds number $Re_{\sqrt{K_y}}$ is less than one, where

$$Re_{\sqrt{K_y}} = \frac{\rho_f \langle v_f \rangle \sqrt{K_y}}{\mu_f} \tag{3.14}$$

If the pressure drop and volume averaged streamwise velocity are known, the transverse permeability K_y may be computed via Darcy's law, Equation (2.34), provided that $Re_{\sqrt{K_y}}$ is sufficiently small. In order to compute K_y from the present results, it is necessary to compute the pressure drop corresponding to $Re_{\sqrt{K_y}} = 0$ by linear extrapolation of the data, as the numerical procedure experiences difficulties at very low Reynolds numbers. To illustrate, Darcy's law may be rewritten as

$$-\nabla \langle p_f \rangle^f \left(\frac{d^2}{\mu_f \langle v_f \rangle} \right) = \frac{d^2}{K_y} \tag{3.15}$$

where the left hand side of the above expression is defined as the nondimensional pressure gradient, $-\nabla p^*$. The permeability for a given fluid volume fraction is

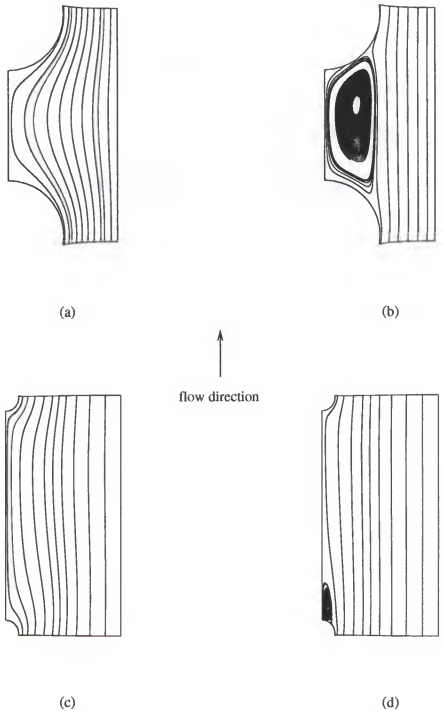

Figure 3.5: Streamline plots for square array – (a) $\epsilon_f = 0.80$, $Re_d = 3.26$ ($Re_{\sqrt{K_y}} = 0.904$); (b) $\epsilon_f = 0.80$, $Re_d = 161$ ($Re_{\sqrt{K_y}} = 44.6$); (c) $\epsilon_f = 0.99$, $Re_d = 4.24$ ($Re_{\sqrt{K_y}} = 13.3$); (d) $\epsilon_f = 0.99$, $Re_d = 105$ ($Re_{\sqrt{K_y}} = 331$).

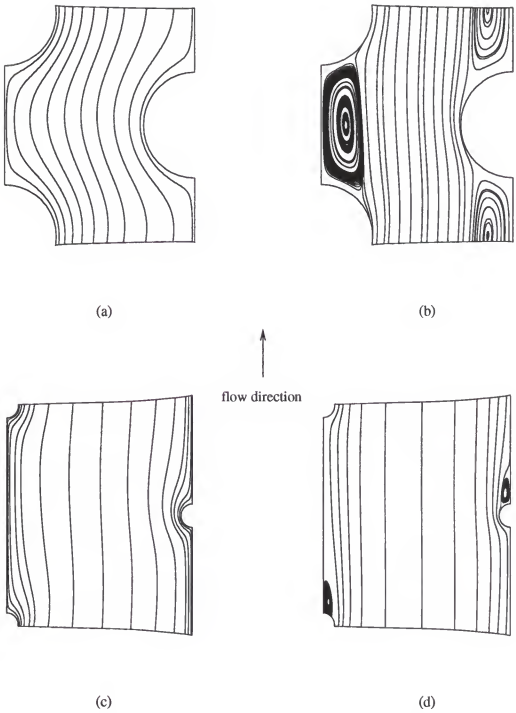

Figure 3.6: Streamline plots for triangular array – (a) $\epsilon_f = 0.80$, $Re_d = 3.01$ ($Re_{\sqrt{K_y}} = 0.849$); (b) $\epsilon_f = 0.80$, $Re_d = 71.5$ ($Re_{\sqrt{K_y}} = 20.1$); (c) $\epsilon_f = 0.99$, $Re_d = 3.89$ ($Re_{\sqrt{K_y}} = 12.4$); (d) $\epsilon_f = 0.99$, $Re_d = 86.6$ ($Re_{\sqrt{K_y}} = 277$).

found by computing $-\nabla p^*$ for data points 1 and 2 at low Reynolds number, and then extrapolating to $Re_d = 0$:

$$\frac{(-\nabla p^*)_2 - (-\nabla p^*)_1}{(Re_d)_2 - (Re_d)_1} = \frac{(-\nabla p^*)_1 - (-\nabla p^*)_o}{(Re_d)_1 - 0} \tag{3.16}$$

Once $(-\nabla p^*)_o$ is computed, the permeability may be found from Equation 3.15. Figure 3.7 shows a plot of the transverse Darcy number, $Da_y = K_y/d^2$, versus the fluid volume fraction for both array types. A comparison is made to the results of Drummond and Tahir [16], who conducted a Stokes flow analysis to obtain closed-form solutions for the permeability of various arrays (similar findings can be found in Clague and Phillips [14] and Sangani and Acrivos [46]). Since the fluid volume fraction is large, little difference can be seen between square and triangular array results. There is excellent agreement (less than 5% relative difference) between the current study and the Stokes flow solutions, which shows that the numerical procedure is accurate for the low Reynolds number range. Another implication of this comparison is that the present numerical procedure, which has difficulty in efficiently yielding accurate results in the creeping flow regime, can still be used to compute permeability to a high degree of accuracy. Thus, future studies of flows in other types of porous media could use computational fluid dynamics (CFD) analysis to determine permeability.

To evaluate the validity of the present results at higher Reynolds number, frictional losses in one row of a periodic array are compared against those reported in the literature. Figure 3.8 shows the nondimensional pressure gradient versus the particle Reynolds number for the square array with $\epsilon_f = 0.80$. Two additional investigations, which are finite element-based numerical studies, are used for comparison: Edwards et al. [19]; and Ghaddar [25]. (Studies where $\epsilon_f > 0.80$ could not be found in the literature for the Reynolds numbers considered.) There is good agreement between the present study and the other numerical results, especially at low Reynolds number. The slight difference at higher Reynolds number can be

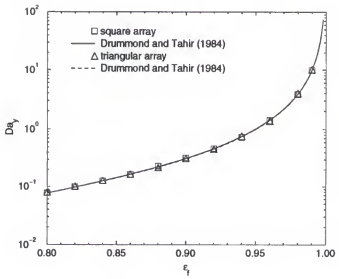

Figure 3.7: Darcy number versus fluid volume fraction for square and triangular arrays.

partly explained by unsteady effects. Ghaddar [25] performed a transient analysis and found inherently unsteady flows to exist for $Re_d > 150$ for this array. However, the relative percent difference in $-\nabla p^*$ between the present study and Ghaddar [25] (about 10%) suggests that unsteady effects are only slightly significant here.

Prior to the presentation of results for the full range of ϵ_f studied, the functional form of the pressure losses in porous media is considered in more detail. The pressure gradient $-\nabla\langle p_f\rangle^f$ for a given array can, in principle, be written as a function of the following variables: ρ_f, μ_f, $\langle v_f\rangle$, d, and K_y. The Buckingham-Pi theorem may be used to determine the nondimensional groups that characterize this relationship: the Darcian Reynolds number, $Re_{\sqrt{K_y}}$; the Darcy number, Da_y; and the modified friction factor, f', where

$$f' = -\nabla\langle p_f\rangle^f \frac{\sqrt{K_y}}{\rho_f \langle v_f\rangle \cdot |\langle v_f\rangle|} \tag{3.17}$$

(The square of the volume averaged velocity is written as $\langle v_f\rangle \cdot |\langle v_f\rangle|$ since the flow may be oriented either in the positive or negative y direction.) Both the Ergun and Forchheimer relations, Equations (2.37) and (2.38), can be rearranged to display

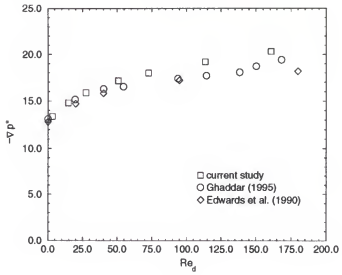

Figure 3.8: Nondimensional pressure gradient versus particle Reynolds number for square array, $\epsilon_f = 0.80$.

the dependence of the frictional losses on these non-dimensional parameters. For example, the Forchheimer equation may alternatively be written as [6]

$$f' = 1/Re_{\sqrt{K_y}} + F_y \tag{3.18}$$

(Ergun's equation may be written similarly.)

To examine the validity of the Ergun and Forchheimer relations, the modified friction factor is plotted versus the Darcian Reynolds number for the square array and the triangular arrays in Figure 3.9 on a logarithmic scale. Both Darcy's law and the Forchheimer relation are shown, with $F_y = 0.00251$ for the square array and 0.00412 for the triangular array. (Values for F_y were determined from the highest $Re_{\sqrt{K_y}}$ for each array type, since a linear regression yielded relative deviations well over 100%.) Several important features can be seen in this figure. First, the data reduces to the Darcy limit as $Re_{\sqrt{K_y}}$ approaches unity, as expected. However, the frictional losses clearly do not follow the Ergun and Forchheimer relations as the Darcian Reynolds number increases. The maximum relative difference between the present data and the Forchheimer relation is 25% for the square array and 66% for

Table 3.2: Correlation values for modified friction factor.

Array Type	b	m	n
Square	0.862	-0.882	0.555
Triangular	0.815	-0.836	1.21

the triangular array. This finding calls into question the validity of the Forchheimer and Ergun expressions for flows in porous media composed of cylinder arrays with large c/d ratios. Previous studies [5] have shown that, for certain classes of porous media, the modified friction factor exhibits little dependence upon the fluid volume fraction. Current results illustrate that ϵ_f has a significant influence upon f', as shown by the scatter in the data points in this figure. To account for the fluid volume fraction dependency, a power-law relationship is proposed as the functional form of f' for $Re_{\sqrt{K_y}} > 1$:

$$f' = b\epsilon_f^{-n} Re_{\sqrt{K_y}}^{m} \tag{3.19}$$

Figure 3.10 illustrates the fidelity of the above correlation for square and triangular arrays, respectively, by plotting the product $f'\epsilon_f^n$ versus $Re_{\sqrt{K_y}}$. The data matches the correlation to within a maximum relative difference of 6.5% for the square array and 4.5% for the triangular array; values of the correlation constants are provided in Table 3.2. The larger value of n for the triangular array suggests a stronger dependence on fluid volume fraction, explained by the more tortuous flow path of this array type. For the triangular array, the tortuosity of the flow path is greatly exacerbated by a decrease in porosity, while a more open flow area exists for the square array. Hence, f' shows more sensitivity to the fluid volume fraction for the triangular array. Both arrays show comparable dependency upon $Re_{\sqrt{K_y}}$, although the modified friction factor is higher for the triangular array for the reasons outlined above.

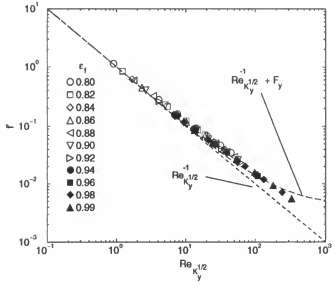

(a)

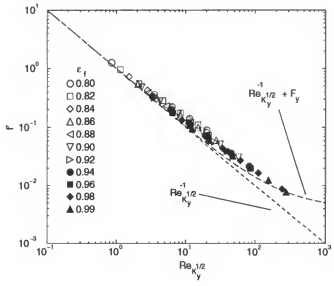

(b)

Figure 3.9: Modified friction factor versus Darcian Reynolds number – (a) square array; (b) triangular array.

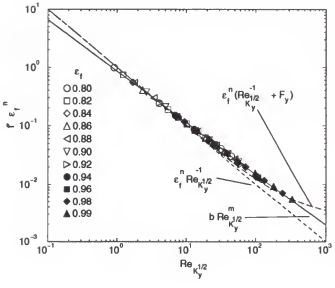

(a)

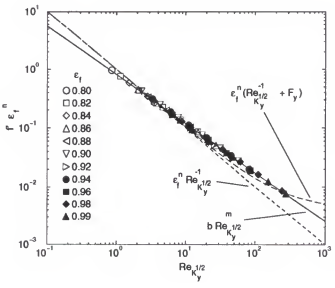

(b)

Figure 3.10: Modified friction factor, as a function of fluid volume fraction, versus Darcian Reynolds number – (a) square array; (b) triangular array.

3.2.3 Results: Heat Transfer

Heat transfer effects are seen in Figures 3.11 and 3.12, which show isotherms for square and triangular arrays considering extreme values of fluid volume fraction and Reynolds number. The isotherms display symmetric shapes for low Reynolds number flows, showing the dominance of conduction over convection. At high Reynolds numbers, isotherms in open flow areas are aligned parallel to the y axis, with more complicated patterns appearing in the recirculation zones. Also, much sharper temperature gradients appear closer to the cylinders as the Reynolds number increases.

To evaluate convective heat transfer, the Nusselt number, Nu_y, is defined as

$$Nu_y = \frac{hd}{k_f} \tag{3.20}$$

The convective heat transfer coefficient h is determined from Equation (2.39), with $T_s = \langle T_s \rangle^s$ and $T_r = \langle T_f \rangle^f$. (It should be noted that T_r is conventionally taken as the fluid bulk temperature; however, $\langle T_f \rangle^f$ is chosen for convenience. Calculations of the Nusselt number based on the bulk temperature revealed only small differences.) For the case of constant wall temperature, q_s is found via an energy balance between the inlet and outlet of the fluid domain and the cylinder walls. Figure 3.13 shows the Nusselt number versus the particle Reynolds number for both array types ($\langle T_s \rangle^s =$ 300 K for constant wall temperature, and $q_s = 2.12 \times 10^{-4}$ W/m^2 for constant wall heat flux). The fluid volume fraction clearly has a strong influence on the degree of heat transfer, as Nu_y rises when the cylinders are closer to each other. There is also a marked dependency upon the wall heating condition, with the constant wall heat flux condition exhibiting Nusselt numbers that are about 20% higher than the constant wall temperature case. A power-law correlation is used as a fit for the data,

$$Nu_y = gRe_d{}^r \tag{3.21}$$

This correlation is considered to be a first approximation, as the results show that the values of coefficients g and r are not independent of Re_d. Tables 3.3 and 3.4 list

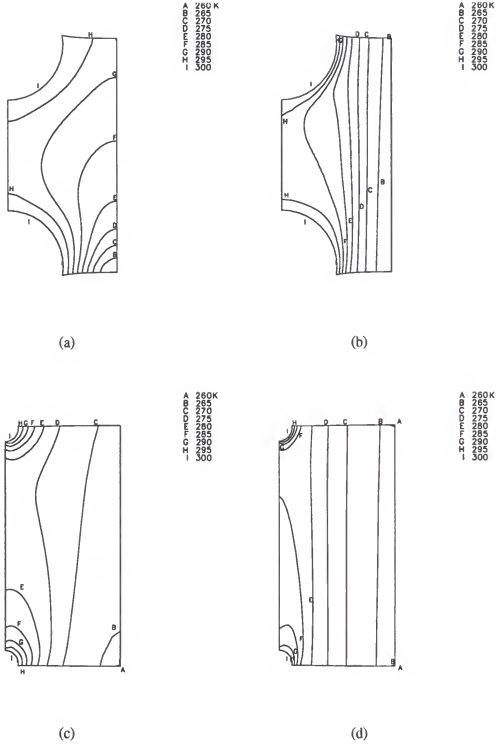

Figure 3.11: Isotherm plots for square array, $\langle T_s \rangle^* = 300$ K – (a) $\epsilon_f = 0.80$, $Re_d = 3.26$ ($Re\sqrt{K_y} = 0.904$); (b) $\epsilon_f = 0.80$, $Re_d = 161$ ($Re\sqrt{K_y} = 44.6$); (c) $\epsilon_f = 0.99$, $Re_d = 4.24$ ($Re\sqrt{K_y} = 13.3$); (d) $\epsilon_f = 0.99$, $Re_d = 105$ ($Re\sqrt{K_y} = 331$).

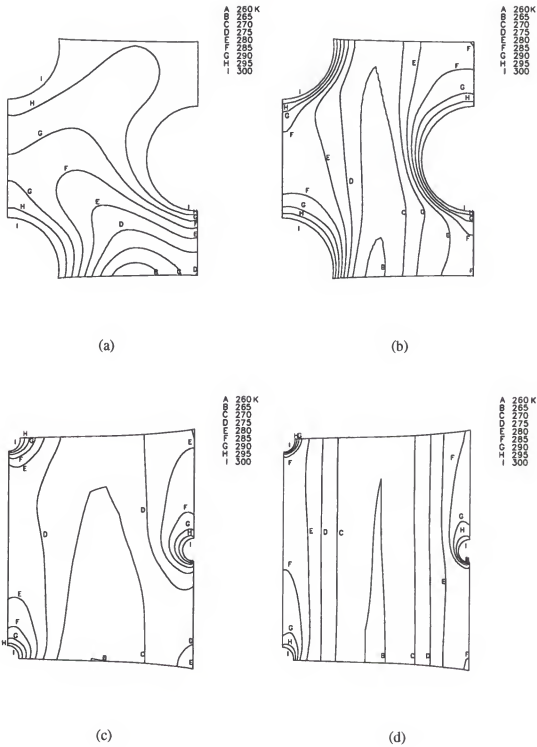

Figure 3.12: Isotherm plots for triangular array, $\langle T_s \rangle^s = 300$ K – (a) $\epsilon_f = 0.80$, $Re_d = 3.01$ ($Re_{\sqrt{K_y}} = 0.849$); (b) $\epsilon_f = 0.80$, $Re_d = 71.5$ ($Re_{\sqrt{K_y}} = 20.1$); (c) $\epsilon_f = 0.99$, $Re_d = 3.89$ ($Re_{\sqrt{K_y}} = 12.4$); (d) $\epsilon_f = 0.99$, $Re_d = 86.6$ ($Re_{\sqrt{K_y}} = 277$).

the coefficients for the square and triangular arrays as a function of the fluid volume fraction for each heating condition (δ_m is the maximum relative difference between actual and correlation values). The relatively moderate values of the Nusselt number suggest that departure from LTE may be significant in those cases where non-equilibrium effects are suspected. However, it is not possible to generally assess the importance of the LTE assumption from the Nusselt number alone, since the interfacial area a_{fs} can attain very large values even for high porosities. Macroscopic analyses similar to the investigation of Amiri and Vafai [2], along with the Nusselt number correlations presented herein, can be used to assess LTE for flows in porous media consisting of cylinder arrays.

Finally, it should be noted that an attempt was made to utilize $\sqrt{K_y}$ as a length scale for heat transfer in order to determine if the data could be represented as a function of the Darcian Reynolds number or as a Nusselt number based on $\sqrt{K_y}$. While application of the Buckingham-Pi theorem to heat transfer reveals dependency on dimensionless groups Re_d, Nu_y, and Da_y, there is no guarantee that the functional relationship is analogous to that found for the modified friction factor. This attempt yielded no conclusive evidence of universal behavior in the Nusselt number as a function of the fluid volume fraction. Hence, the results have been presented in the more traditional fashion with the cylinder diameter as the length scale.

3.3 Yawed Flows

In some instances it is possible that the flow through a cylinder array is neither parallel nor transverse to the array. Instead, the local macroscopic velocity vector may be aligned at a yaw angle Ψ between 0° and 90°, as measured from the cylinder axis (0° represents parallel flow and 90° represents transverse flow). Considering the macroscopic momentum terms, this situation represents no difficulty. Since $\boldsymbol{M}_f$ is a vector, separate components represent parallel and transverse resistances,

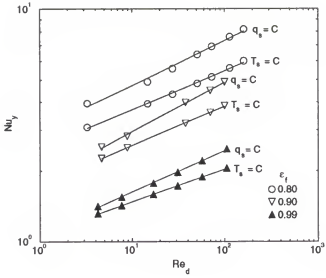

(a)

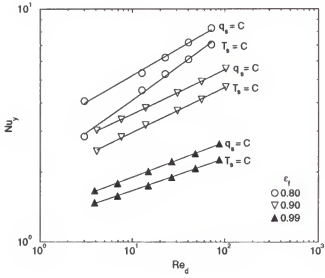

(b)

Figure 3.13: Nusselt number versus particle Reynolds number – (a) square array; (b) triangular array.

Table 3.3: Correlation values for Nusselt number, square array.

	$T_s = C$			$q_s = C$		
ϵ_f	g	r	δ_m (%)	g	r	$\lvert\delta_m\rvert$ (%)
0.80	2.50	0.170	1.4	3.05	0.191	3.8
0.82	2.38	0.166	1.0	2.78	0.192	3.1
0.84	2.21	0.169	1.2	2.47	0.204	2.3
0.86	2.04	0.171	0.8	2.19	0.212	1.4
0.88	1.87	0.174	0.9	2.03	0.210	2.2
0.90	1.73	0.172	0.7	1.79	0.218	1.9
0.92	1.60	0.167	0.4	1.57	0.221	1.0
0.94	1.46	0.162	0.6	1.37	0.227	0.7
0.96	1.35	0.147	0.2	1.26	0.207	0.9
0.98	1.18	0.138	0.3	1.13	0.193	1.7
0.99	1.07	0.140	0.5	1.08	0.177	1.2

Table 3.4: Correlation values for Nusselt number, triangular array.

	$T_s = C$			$q_s = C$		
ϵ_f	g	r	δ_m (%)	g	r	$\lvert\delta_m\rvert$ (%)
0.80	2.12	0.286	3.0	3.11	0.226	3.1
0.82	2.12	0.268	1.9	2.87	0.226	1.8
0.84	2.10	0.245	1.4	2.70	0.221	1.1
0.86	2.06	0.225	1.0	2.46	0.224	1.2
0.88	2.00	0.209	0.7	2.16	0.256	2.2
0.90	1.89	0.196	1.2	2.31	0.189	0.7
0.92	1.81	0.176	0.5	2.17	0.175	0.2
0.94	1.68	0.162	0.4	2.01	0.163	0.8
0.96	1.54	0.146	0.3	1.80	0.154	0.7
0.98	1.34	0.143	1.2	1.56	0.150	1.2
0.99	1.21	0.138	0.8	1.35	0.150	0.6

according to the alignment of the array with respect to the particular coordinate system. Hence, the net flow resistance in a direction parallel to Ψ is computed by the vectorial sum of the components of $\boldsymbol{M}_f$. It is implied that off-diagonal terms of the momentum source term are zero, which is an assumption commonly used in porous media modeling [3, 4]. On the other hand, the energy source term E_f is a scalar quantity, so a different approach must be taken for this term. Rather than conducting microscopic analyses in order to determine the interfacial heat transfer coefficient for yawed flows, the value of h_{fs} can be approximated from knowledge of the heat transfer characteristics for parallel and transverse flows. Based on experimental results from yawed flows over single long cylinders, Morgan [40] presented the following correlation for the Nusselt number, $Nu = h_{fs}d/k_f$:

$$Nu = \left(Nu_y^4 \sin^2\Psi + Nu_z^4 \cos^2\Psi\right)^{\frac{1}{4}} \tag{3.22}$$

In this expression, Nu_y and Nu_z are the Nusselt numbers transverse and parallel to the cylinder array, respectively. For this study, it is assumed that interfacial heat transfer for cylinder arrays is represented by Equation (3.22).

3.4 Concluding Remarks

The specific forms of the macroscopic source terms have been presented for flows parallel and transverse to cylinder arrays. When the flow is longitudinal to the array, the formulations do not depend on Reynolds number because the flow remains attached; hence the momentum and energy source terms are functions of array type and porosity alone. For transverse flow, frictional losses follow Darcy's law when the Darcian Reynolds number is of the order one, but show significant non-Darcy effects as the Reynolds number increases. Comparison to previous numerical studies in square arrays reveals few differences, especially at low Reynolds number. The modified friction factor is shown to follow a power-law function of Darcian Reynolds number rather than the Ergun or Forchheimer relations, with strong dependency

on the fluid volume fraction. Nusselt number correlations utilizing the cylinder diameter as the length scale are also derived via a power-law relationship.

CHAPTER 4
CONVECTIVE AND RADIATIVE HEAT TRANSFER ENHANCEMENT WITH FIBER ARRAY INSERTS IN TUBE FLOW

With the macroscopic source terms already determined, it is now possible to examine the influence of fiber array inserts for heat transfer augmentation. The first application of fiber array inserts to be presented in this study considers inserts filling a circular tube, as proposed by Im and Ahluwalia [31]. These researchers explored the use of fiber array inserts aligned longitudinally to the pipe axis, with a number of fiber materials selected to determine which offered the best performance. As an introductory study, the Im and Ahluwalia investigation [31] provided strong evidence of heat transfer enhancement and the resulting pressure losses in fiber filled tubes. Based on these positive results, a more in-depth investigation is merited; one which analyzes fiber/fluid interaction more closely. In particular, because the interest is in highly porous inserts and only the fibers are active in radiation transfer (the fluid does not participate), local thermodynamic equilibrium between the fluid and fibers must be examined.

In this chapter, an analysis is presented which considers conduction, convection, and radiation within a two-dimensional axisymmetric domain. Silicon carbide (SiC) is selected as the fiber material, as it was identified by Im and Ahluwalia [31] as having the best radiative characteristics out of a number of ceramic and metallic compounds. The analysis of Im and Ahluwalia [31] is extended by detailed numerical simulations which account for multidimensional effects and the macroscopic coupling of the heat transfer modes. In addition, emphasis is placed on pipe wall temperature

reduction as a performance criteria. The sensitivity of porosity, ranging from 0.90 to 0.99, is closely studied for a laminar tube Reynolds number of 1000.

4.1 Analysis

Previously, the forms of the momentum and energy source terms were presented for square and triangular cylinder arrays with various porosities. Because square and triangular arrays have similar performance at high fluid volume fractions, only square arrays are considered for this application. A summary of these terms and their use in the tube flow application are presented below. In addition, radiative heat transfer within the fiber array insert is explained in more detail.

4.1.1 Momentum and Energy Source Terms

The momentum source term tensor, $\boldsymbol{M}_f$, for flow longitudinal to the fiber array insert is found by Darcy's law, Equation (2.34), with the permeability K_z given in Equation (3.3) (z is the axial coordinate direction). Non-Darcy effects should not be important in this situation since the radial velocity components are small and flow longitudinal to the fiber array insert does not exhibit any inertial effects due to vortex generation or wakes. (Results showed this statement to be true, as the Darcian Reynolds number in the transverse direction was shown to be much less than one for all cases considered.) The transverse flow component of $\boldsymbol{M}_f$ may also specified by Darcy's law, with the transverse permeability K_r found as follows [3]:

$$\frac{K_r}{C_r} = \frac{d^2}{16\epsilon_s} \tag{4.1}$$

where C_r is [16]

$$C_r = \frac{1}{2}\left(\ln\left(\frac{1}{\epsilon_s}\right) - 1.476 + \frac{2\epsilon_s - 0.796{\epsilon_s}^2}{10.489\epsilon_s - 1.60{\epsilon_s}^2}\right) \tag{4.2}$$

The radial coordinate direction is denoted r, and circumferential variations are ignored.

Since the fluid volume fraction is large, the effective conductivity of the fluid phase is taken as the actual fluid conductivity, or

$$k_{f,r} = k_{f,z} = k_f \tag{4.3}$$

Similar to the fluid phase, the axial conductivity for the solid is

$$k_{s,z} = k_s \tag{4.4}$$

while $k_{s,r} = 0$ because the fibers are not connected radially. The determination of the interfacial heat transfer coefficient h_{fs} is given by Equation (3.22).

4.1.2 Radiative Transport

Since radiative transfer is important in this circumstance, the radiative transport equation (RTE), Equation (2.28), must be solved along with the other macroscopic transport equations. In order to determine the absorption and scattering coefficients, κ_λ and σ_λ, the real and complex indices of refraction, n and k, must be known for the given fiber material. Palik [43] present the optical properties for a number of solid materials, including SiC. An oscillator model is reported to be in good agreement with experimental results in the 2-22 μm range:

$$(n - ik)^2 = \epsilon_\infty \left(1 + \frac{\omega_L^2 - \omega_T^2}{\omega_T^2 - \omega^2 + i\omega_\Gamma \omega}\right) \tag{4.5}$$

where ω is the wavenumber $(1/\lambda)$, $\omega_L = 969$ cm^{-1}, $\omega_T = 793$ cm^{-1}, $\omega_\Gamma = 4.76$ cm^{-1}, and $\epsilon_\infty = 6.7$ (considering the parallel polarized, or ordinary, ray). Figure 4.1 illustrates n and k as a function of wavelength for SiC. It can be seen that the optical properties are a strong function of wavelength, with an abrupt change in n and k shown around 10 μm. Next, the absorption efficiency factor Q_a is found from solution of the electromagnetic wave equation. Following Bohren and Huffman [9], the wavelength dependence of Q_a is computed as a function of the size parameter $x = \pi d/\lambda$ and optical properties n and k (see inset of Figure 4.2). The absorption

coefficient κ_λ is related to the absorption efficiency factor by [39]

$$\kappa_\lambda = Q_a \left(\frac{4\epsilon_s}{d} \right) \tag{4.6}$$

The stepwise gray approximation [39] is used to simplify the nongray treatment, and Q_a is subdivided into five zones as shown in Figure 4.2. Zones I, III, and V have constant κ_λ values, with $\kappa_\mathrm{I} = 0$ (i.e. transparent) in Zone I, and κ_V in Zone V extrapolated from Zone IV. (The assumption for Zone V is necessary since n and k for SiC in this particular wavelength region could not be found in the literature. As shown in Figure 4.1, n appears to level off as the wavelength increases, while k continues to decrease, hence Q_a is extrapolated here. Although the correctness of this assumption is debatable, the blackbody fraction corresponding to Zone V is less than 10% for temperatures above 500 K.) Zones II and IV exhibit gas-like absorptive behavior, hence a special procedure is employed to determine κ for each of these zones. As described by Modest [39], κ and the bandwidth $\Delta\lambda$ are chosen so that the stepwise gray approximation predicts the correct band absorptance for both optically thin and optically thick situations. Thus, κ and $\Delta\lambda$ for these zones are found via the following relations: optically thin limit,

$$\int \kappa_\lambda d\lambda = \kappa \Delta\lambda \tag{4.7}$$

and optically thick limit,

$$\int \left(1 - e^{-\kappa_\lambda X_m}\right) d\lambda = \Delta\lambda \left(1 - e^{-\kappa X_m}\right) \tag{4.8}$$

where X_m is the mean beam length of the media, taken as $0.94D$ for an infinite circular cylinder [39]. Figure 4.2 shows κ for each of the four radiatively participating zones as a function of porosity.

Considering a wavelength of 10 μm as a reference value in the thermal band, the clearance-to-wavelength ratio, c/λ, is of order ten for fibers with $d = 150\mu$m. Thus, the assumption of independent scattering is valid here. Scattering of radiation

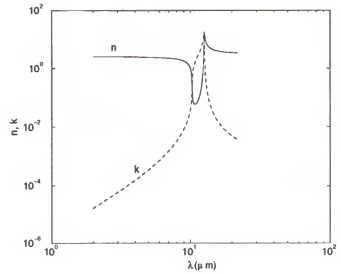

Figure 4.1: Optical properties of SiC versus wavelength.

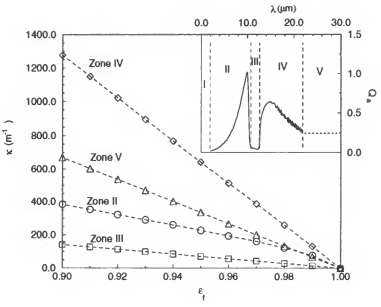

Figure 4.2: Absorption coefficient versus fluid volume fraction for SiC fibers, $d = 150\ \mu$m (inset: absorption efficiency factor versus wavelength).

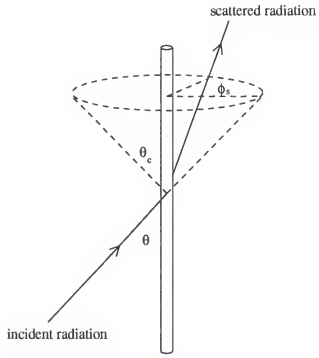

Figure 4.3: Scattering of radiation from a fiber.

from a single fiber has been studied by a number of researchers [22, 35, 66], and is shown in Figure 4.3. The pencil ray is shown to have an incident angle θ, and the scattered radiation is contained within a cone that has an apex angle $\theta_c = \theta$. Angle ϕ_s is the scattering angle as measured from the horizontal projection of the incident ray. Rather than using the complicated Mie scattering theory to determine the scattering phase function, the diffraction theory approximation is invoked since the size parameter, x_R, is large ($x_R \sim \mathcal{O}(10^1)$). Figure 4.4 shows the scattering phase function Φ_λ for a given scattering angle ϕ_s, as calculated by the diffraction theory approximation [9]:

$$\Phi_\lambda(\phi_s) = \frac{\pi}{4x}\left[\left(\frac{1+\cos\phi_s}{\pi}\right)\left(\frac{\sin(x_R\sin\phi_s)}{\sin\phi_s}\right)\right]^2 \tag{4.9}$$

For the two size parameters shown in the figure, which represent values in Zones II and IV, Φ_λ is shown to be highly forward scattering. Therefore, out-scattering is neglected in this study, resulting in $\sigma_\lambda = 0$ and $\beta_\lambda = \kappa_\lambda$.

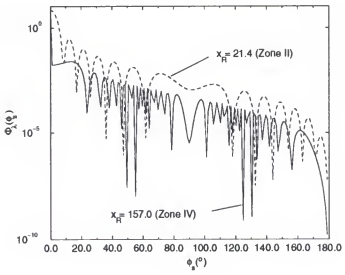

Figure 4.4: Scattering phase function versus scattering angle for SiC fibers, $d = 150$ μm.

4.1.3 Numerical Approach

A finite volume-based numerical procedure based on the SIMPLE algorithm [44] is used to solve the macroscopic equations, Equations (2.42) – (2.47), in two-dimensional axisymmetric coordinates r and z, with the hybrid scheme [44] used for convective terms. The solution procedure to the RTE is described in Moder et al. [38], with slight modification made to the treatment of the spatial grid in the circumferential direction, γ. In the method described by Moder et al. [38], which is based on the control volume formulation of Chai [11] presented in Chapter 2, a fixed number of control volumes is required to span the entire circumferential direction $0 < \gamma < 2\pi$. Alternatively, a single control volume with size $\Delta\gamma$ may be employed if rotational symmetry is applied at the boundaries. This scheme is used for the present analysis, as shown in Figure 4.5. In order to produce accurate results, $\Delta\gamma$ and the azimuthal control volume $\Delta\phi$ are sized so that the ratio $\Delta\gamma/\Delta\phi$ equals an integer equal to or greater than one. This requirement eliminates the necessity for interpolation of the intensity at the east and west boundaries. The step scheme is

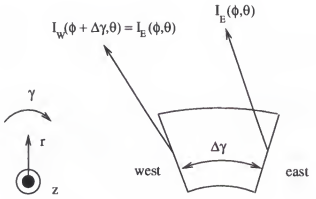

Figure 4.5: Design of axisymmetric boundary conditions for radiative transfer.

used to determine the value of the outgoing radiation [11, 38], which is I_W in Figure 4.5(b), and the incident intensity is computed by rotational symmetry:

$$I_E(\phi,\theta) = I_W(\phi + \Delta\gamma,\theta) \tag{4.10}$$

where $\Delta\gamma/\Delta\phi = 1$. For the present computations, the angular grid is divided into 8 $\times$ 16 control volumes in the θ and ϕ directions, and the spatial grid is divided into 10 $\times$ 40 control volumes in the radial and axial directions, respectively.

To check the validity of the model, the numerical study presented by Einstein [20] is selected as one benchmark. This study considers a radiatively participating gray gas flowing through a pipe with black walls and constant wall temperature (750 K); the inlet and outlet of the pipe are black, with T_i = 300 K. Figure 4.6 shows a comparison to the Einstein study, which features the nondimensional outlet temperature versus optical depth for a number of conduction-to-radiation ratios. The present results show a variation of no more than 5% from values reported by Einstein. In addition, the accuracy of the radiation calculations is checked against results presented in Chui et al. [13], who determined an exact solution to radiative transfer in a cylindrical enclosure with cold, black walls and uniform (gray) medium temperature. The nondimensionalized wall heat flux is shown in Figure 4.7 as a function of axial location. Good agreement (less than 5% deviation) can be seen for three optical depths shown, with the current results approaching the exact solution

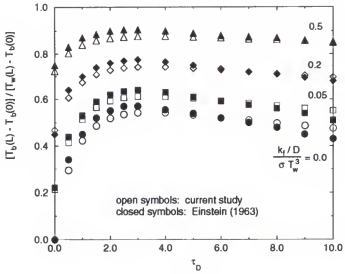

Figure 4.6: Nondimensional outlet temperature versus optical depth for radiatively participating gas flow ($L/D = 5.0, Re_D = 1309, T_w = 750$ K, and $T_i/T_w = 0.4$).

as the azimuthal angular discretization is further refined. (It should be noted that the spatial grid is 16 × 30 for this comparison.)

For the present application, no-slip and no-penetration boundary conditions are imposed at the tube wall, with the outlet velocity extrapolated in the streamwise direction. The inlet and outlet of the tube are black, and a constant heat flux $q_w = 1800$ W/m^2 is applied to the tube wall, which has a total hemispherical emissivity indicative of unpolished metals ($\bar{\epsilon}_w = 0.3$ [39]). The inlet fluid temperature is fixed at 300 K, and the outlet fluid temperature, along with the inlet and outlet solid temperatures, are extrapolated from the interior. Fluid and solid are considered to be isothermal at the tube wall, and the wall temperature is found via a balance of the wall heat flux, conduction and radiation. This energy balance may be expressed as follows:

$$q_w = q_R - k_f \frac{\partial T_w}{\partial r} \tag{4.11}$$

where the net radiative heat flux q_R is

$$q_R = \int I(\vec{s} \cdot \pm\vec{n}_r) d\Omega \tag{4.12}$$

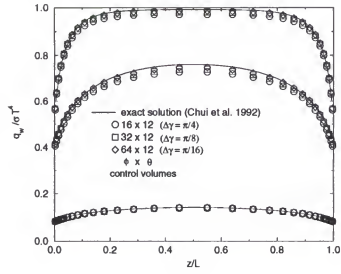

Figure 4.7: Nondimensional wall heat flux versus nondimensional axial length for radiative heat transfer in a cylindrical enclosure with cold walls and uniform medium temperature ($L/D = 1.0$).

($\pm\vec{n}_r$ is the unit normal vector at the wall). The wall temperature T_w is explicitly computed at every iteration from Equation (4.11) by first-order differencing of the conduction term. A tube Reynolds number, Re_D, of 1000 is considered, with a fully developed laminar (parabolic) profile assigned at the inlet. The physical properties of the fluid (air) and SiC are taken at 300 K, and can be found in Incropera and DeWitt [32]; see Table 4.1 for their values, along with other input parameters.

4.2 Results

One consequence of employing fiber array inserts is the alteration of the velocity profile due to the strong flow resistance offered by the porous media. Figure 4.8 illustrates the nondimensional centerline velocity u_c^* as a function of axial length for a range of porosity values. The value of u_c^* is defined as

$$u_c^* = \frac{\langle u_f(0,z)\rangle}{U} \tag{4.13}$$

where $\langle u_f(0,z)\rangle$ is axial centerline velocity and U the average axial velocity. For

Table 4.1: Input parameters for fiber array insert analysis.

Parameter	Value
ρ_f	1.23 kg/m^3
μ_f	1.79×10^{-5} N-s/m^2
$c_{p,f}$	1006 J/kg-K
k_f	0.025 W/m-°C
k_s	490 W/m-°C
T_i	300 K
D	0.025 m
L	0.5 m
Re_D	1000
q_w	1800 W/m^2

a porosity of one, the centerline velocity is twice the average velocity, resulting from the fully developed laminar profile. Addition of fiber array inserts tends to flatten out the flow within a certain entry length, which becomes very short as the porosity is reduced. To illustrate the spreading of the flow as the porosity is reduced, representative velocity profiles at location $z/L = 0.2$ are shown in Figure 4.9.

In order to quantify the heat transfer enhancement, a heat exchange effectiveness $\Theta(z)$ is defined as

$$\Theta(z) = \frac{T_b(z) - T_b(0)}{T_w(z) - T_b(z)} \tag{4.14}$$

where $T_b(z)$ and $T_w(z)$ are the bulk and wall temperatures for axial location z. The heat exchange effectiveness represents the ratio of the actual heat transfer to the fluid to the maximum possible heat transfer at a given axial location. Figure 4.10 shows the heat exchange effectiveness at the tube outlet $z = L$ as a function of porosity and optical thickness, where τ_D is based on the Planck-mean absorption coefficient, $\overline{\kappa}$, evaluated at 580 K. Six different curves of $\Theta(L)$ are shown to illustrate the importance of the heat transfer modes and modeling assumptions, which can be classified as follows: radiative transfer (with conduction and convection) versus no radiative transfer (i.e. conduction and convection alone); nongray versus gray ra-

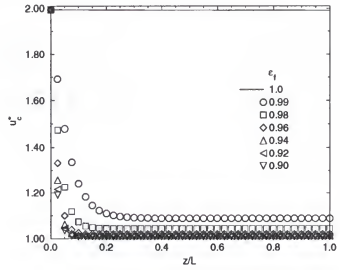

Figure 4.8: Nondimensional centerline fluid velocity versus nondimensional axial length.

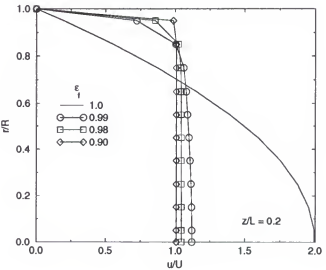

Figure 4.9: Radial coordinate versus streamwise velocity at $z/L = 0.2$.

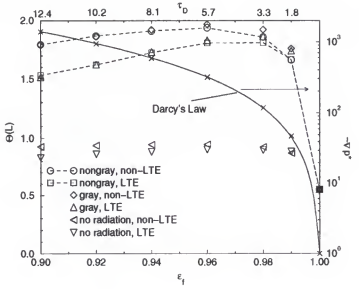

Figure 4.10: Heat exchange effectiveness and nondimensionalized pressure drop at tube outlet versus fluid volume fraction.

diative transfer; and local thermodynamic equilibrium (LTE) versus nonequilibrium (denoted non-LTE). The figure shows that the radiative mode of heat transfer is responsible for a significant portion of the heat transfer augmentation. Nongray effects are most important in the optically thin region, while at higher optical depths the difference between gray and nongray radiative transfer is indistinguishable. Also, the results illustrate the importance of nonequilibrium effects, especially at higher optical depths. For the case of nongray radiative transfer with the non-LTE assumption, an optimum in $\Theta(L)$ can be seen at $\tau_D = 5.7$, showing the self-shielding effect which is evident as the fiber array insert becomes strongly absorbing. With respect to the case of conduction and convection alone, the sharp increase in $\Theta(L)$ as $\epsilon_f \rightarrow 1.0$ can be attributed to the change in velocity profile from parabolic to flat. The importance of relaxing the LTE assumption for the no radiation case can also be seen, although to a lesser degree.

To assess the pressure drop penalty introduced by the fiber array inserts, a nondimensionalized pressure gradient $-\nabla p^*$ is defined as:

$$-\nabla p^* = \frac{-\nabla \langle p_f \rangle^f}{-\nabla p_h} \tag{4.15}$$

representing the ratio of the pressure gradient with the fiber array inserts to the pressure gradient for homogeneous (no fiber) flow. The value of $-\nabla p^*$, also shown in Figure 4.10, rises monotonically as the porosity is reduced, attaining values on the order of ten to one thousand times the homogeneous pressure gradient. (At the optimum value of $\Theta(L)$, $-\nabla p^* = 316$.) The comparison to $-\nabla p^*$ as computed by Darcy's law shows that hydraulic entry length effects are not appreciable in this application.

It is also of interest to evaluate heat transport downstream of the inlet of the tube. As shown in Figure 4.11, the heat exchange effectiveness $\Theta(z)$ varies axially for a number of different porosities, with comparison made to the radiation versus no radiation cases. For the case with radiative transfer included, $\Theta(z)$ initially rises sharply as the porosity is reduced. However, the self-shielding effect mentioned previously becomes more substantial further downstream as temperatures rise. When radiation is not included, the change in the velocity profile causes a sudden rise in $\Theta(z)$ at the inlet. The dependency of $\Theta(z)$ with porosity can be attributed to the influence of fiber array insert conductivity at larger solid volume fractions. Leveling off of $\Theta(z)$ at the tube outlet results from the zero gradient boundary condition.

To evaluate the reduction in wall temperature, the nondimensional tube wall temperature, $T_w^*(z) = T_w(z)/T_i$, is shown in Figure 4.12 as a function of axial location. At the inlet, little differences can be seen between the radiation and no radiation cases. However, the importance of radiative transfer appears further downstream as this mode of heat transfer becomes more dominant. At the outlet, a significant reduction in wall temperature (about 30% with radiation) is achieved with fiber array inserts, even for porosities as high as 0.99. This finding shows

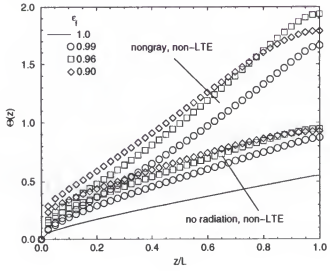

Figure 4.11: Heat exchange effectiveness versus nondimensional axial length.

that high porosity fiber array inserts can be employed for applications where only a moderate reduction in wall temperature is required, hence minimizing the pressure drop penalty.

4.3 Concluding Remarks

The present study confirms that convective and radiative internal heat transfer augmentation with fiber array inserts has great potential as a technique for use in novel heat exchange devices. For the specified parameters, the heat exchange effectiveness was more than tripled with the fiber array inserts as compared to homogeneous flow, resulting in a 30% reduction in tube wall outlet temperature. Although LTE was apparent in the case of conduction and convection alone, significant departure from this assumption could be seen when radiation was included. This finding illustrates the influence of non-LTE effects in cases where radiation is important. The final merits of the fiber array insert must, of course, be determined from an

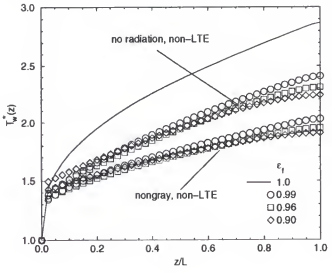

Figure 4.12: Nondimensional tube wall temperature versus nondimensional axial length.

overall performance analysis with respect to the given application, especially since the pressure drop penalty is large.

CHAPTER 5
CONVECTIVE HEAT TRANSFER ENHANCEMENT WITH FIBER ARRAY INSERTS IN RECIRCULATING FLOWS

The previous chapter demonstrated that fiber array inserts yield substantial increases in heat transfer rates, but are accompanied by significant frictional losses. In contrast to flow in straight tubes, the need for heat transfer enhancement is often driven by the appearance of recirculation zones, which can cause 'hot spots' to occur. For these situations, fiber array inserts can be utilized to alter the flow field so that recirculation zones are reduced in size. Because of the strong flow resistance offered by fiber array inserts, only a portion of the flow region needs to be filled with the array. As mentioned previously, Hendricks et al. [27] experimentally investigated the use of a brush insert for the reduction of flow separation within a complex cooling passage. The authors qualitatively showed that the insert resulted in favorable changes in the flow field, but did not explore the effects of varying the insert length or porosity. Ichimiya et al. [30] numerically evaluated the role of heat transfer enhancement with porous media in a miter bend. While this study shows the benefits of porous media for heat transfer enhancement, it did not account for cases where the duct is only partially filled.

In order to investigate the influence of short fiber array inserts on the flow field within a simple but well-studied geometry, flow over a backward-facing step is examined, as depicted in Figure 5.1. This situation features one or more recirculation zones downstream of the inlet, depending on the flow Reynolds number. From a heat transfer perspective, the reduction or elimination of recirculation is highly desirable, as wall temperatures are typically very high in these regions. In lieu of smoothing

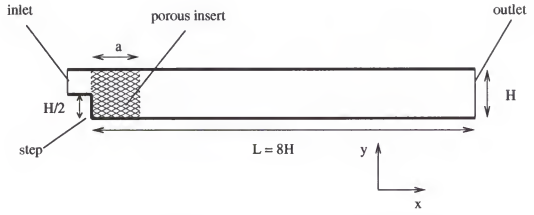

Figure 5.1: Schematic of duct with backward-facing step.

out or extending the abrupt inlet region, one option is to partially fill the duct directly behind the step with a fiber array insert (see Figure 5.1). The resistance to flow offered by the insert changes the streamwise velocity profile, which impacts the formation of recirculation zones beyond the insert. This flow resistance also may prevent the formation of recirculation zones within the porous region itself. In addition, if the insert consists of a high conductivity material with a large specific surface area, the removal of heat in these regions may further be enhanced by insert-wall conduction. Presuming that the porous media consists of a uniform matrix, the porosity, ϵ_f, and the insert length, a, are key factors to the insert performance.

The objective of the investigation presented herein is to explore the use of fiber array inserts for heat transfer enhancement in recirculating flows. Laminar flow over the backward-facing step shown in Figure 5.1 is considered, with a duct Reynolds number Re_H of 800 ($Re_H = \rho U H/\mu$, where U is the average inlet velocity and H is the duct height). The insert consists of a square array of fibers mounted transverse to the streamwise flow, with silicon carbide (SiC) again selected as the fiber material. Although the fiber array has a high porosity ($0.90 \leq \epsilon_f \leq 0.99$), the small diameter of the fibers ($d = 150\mu$m) relative to the duct dimensions results in a large interfacial surface area. A range of insert lengths, ranging from $0.10 \leq a/H \leq 0.25$, are considered for this problem. Since the inserts are short with respect to the

overall size of the domain, radiative transfer is not accounted for in this application. Non-Darcy effects are expected to be important in this application due to the combination of high porosity and large particle Reynolds number. Constant wall heat flux conditions are considered to emphasize the role of the insert in temperature reduction. Since there is a large discrepancy between the fluid and fiber array conductivity, local thermodynamic equilibrium (LTE) in the porous structure is not assumed.

5.1 Problem Description and Numerical Approach

Similar to the axisymmetric case, a finite volume-based numerical procedure based on the SIMPLE algorithm [44] is used to solved the macroscopic equations, Equations (2.42) – (2.45), in a two-dimensional cartesian coordinate system. Central differencing is used for the treatment of convective terms rather than hybrid differencing in order to accurately simulate the more complex flow field. (The order of accuracy for the central differencing scheme is second order, while the hybrid scheme is first order [44, 48]). Treatment of the source terms is the same as in the tube flow application, but non-Darcy flow is now considered (see Chapter 3). Unlike the previous application, where the fiber array filled the entire global domain, in this instance there is an internal interface between the insert and the pure fluid. The macroscopic equations are valid in both regions, of course, but the abrupt change in properties and source terms at the interface requires special consideration. For example, fluid convection features the term $(\rho_f/\epsilon_f^2)\langle\vec{u}_f\rangle \cdot \nabla\langle\vec{u}_f\rangle$ in the momentum equation, which reduces to $\rho_f\langle\vec{u}_f\rangle \cdot \nabla\langle\vec{u}_f\rangle$ in the pure fluid. In effect, the density changes abruptly at the interface region. The effective density at the interface, ρ_i, is found by the harmonic mean [44] of the net densities in the porous media and pure fluid regions:

$$\rho_i = \left(\frac{1 - f_i}{\rho_f/\epsilon_f^2} + \frac{f_i}{\rho_f}\right)^{-1} \tag{5.1}$$

In this expression, f_i is the interpolation factor, which is computed based on the size of the control volumes directly adjacent to the interface region: (i.e., east and west sides):

$$f_i = \frac{\delta x_w}{2\delta x_e} \tag{5.2}$$

Other terms are computed in a similar manner.

Referring to Figure 5.1, the computational domain is divided into a 96×81 grid, with 20 cells located just behind the step along $x/H = 0.5$. No-slip and no-penetration boundary conditions are imposed at the solid walls. The inlet velocity is parabolic (i.e. fully developed), and the Reynolds number based on duct height, Re_H, is 800. At the outlet, the velocity is extrapolated in the streamwise direction, and global mass conservation is used after every iteration (see Shyy [48]). The upper and lower walls are supplied a constant heat flux $q_w = 2.0$ kW/m^2, where both fluid and solid temperatures are taken as the wall temperature, T_w. Furthermore, it is assumed that the fiber array is in good thermal contact with the upper and lower walls, hence T_w is specified via

$$q_w = -(\epsilon_s k_s + \epsilon_f k_f) \left.\frac{\partial T_w}{\partial y}\right|_{y=0,H} \tag{5.3}$$

where contributions from both fluid and solid phases are included in the effective conductivity. The temperatures of the fluid and solid at the inlet and left wall are fixed at T_i, while the outlet is adiabatic. Physical properties of the fluid (air) and the fiber array (SiC) are taken at 300 K, and can be found in Incropera and Dewitt [32] (refer to Table 5.1, which includes the input parameters).

In order to check the validity of the model, results are compared to the investigation of Gartling [24], who performed a detailed study of flow over a backward-facing step. Figure 5.2 shows the u velocity profile, normalized by the inlet velocity U, at a distance of $x/H = 7$ from the step. Excellent agreement can be seen, as results from the present study and Gartling [24] are nearly indistinguishable. Streamlines are shown in Figure 5.3 for this situation, showing a primary recirculation zone along

Table 5.1: Input parameters for analysis of flow over backward-facing step.

Parameter	Value
ρ_f	1.23 kg/m^3
μ_f	1.79×10^{-5} N-s/m^2
$c_{p,f}$	1006 J/kg-K
k_f	0.025 W/m-°C
k_s	490 W/m-°C
T_i	300 K
H	0.025 m
L	0.2 m
Re_H	800
q_w	2.0 kW/m^2

the lower wall, and a secondary recirculation zone along the upper wall near the outlet.

In addition, the numerical study presented by Sparrow et al. [53] has also been selected to validate the present model, with $Re_H = 600$ (here, the lower wall is isothermal, and the upper wall and step are adiabatic). Figure 5.4 shows the development of the u velocity near the bottom wall and the lower wall Nusselt numbers downstream of the step, which are defined as follows:

$$Nu_w = \frac{-\frac{\partial T_w}{\partial y}\Big|_{y=0} H}{T_w - T_b} \tag{5.4}$$

where T_b is the bulk temperature, and

$$Nu_{w,i} = \frac{-\frac{\partial T_w}{\partial y}\Big|_{y=0} H}{T_w - T_i} \tag{5.5}$$

Because a uniform grid distribution is considered for the present study, it is necessary to interpolate for the value of u/U at the transverse location reported by Sparrow et al. ($y/H = 0.00113$), hence there is a slight discrepancy in the velocity profile. However, there is good agreement in the location of the reattachment point. With regards to heat transfer, good agreement is shown up to $x/H \approx 5$, after which the present study predicts higher Nusselt number values. This finding is due to a small

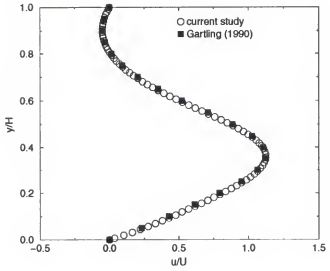

Figure 5.2: Fluid flow in homogeneous duct – transverse coordinate versus streamwise velocity component at $x/H = 7$, $Re_H = 800$.

recirculation zone which was computed by the present model, but not shown to exist by Sparrow et al. [53]. Because these authors do not report the details of their numerical procedure, such as the choice of convection scheme, it is difficult to explain the Nusselt number differences with certainty. However, the reasonable qualitative agreement with Sparrow et al. [53] combined with the excellent correspondence to Gartling [24] demonstrates the fitness of the present numerical procedure.

Finally, the porous media flow equations were compared against the analytical solution reported by Vafai and Thiyagaraja [63] for fully developed porous media flow near a solid wall. The wall velocity u_w, as a function of the dimensionless wall coordinate η, is shown in Figure 5.5 for non-Darcy and Darcy flow conditions. (For this case, the Forchheimer equation was considered for the momentum source term instead of the previously mentioned formulation.) The velocity distribution was found to match within about 2% of the analytical predictions.

Figure 5.3: Fluid flow in homogeneous duct – streamline plot, $Re_H = 800$.

5.2 Results – Fluid Flow

The qualitative impact of the fiber array inserts on the downstream flow is shown in Figures 5.6 and 5.7 as a function of a/H and porosity. Referring to Figure 5.6, the presence of even a high porosity insert ($\epsilon_f = 0.99$) serves to dramatically change the nature of the flow field. With $a/H = 0.10$, the lower wall recirculation zone nearly fills the entire duct, which is in contrast to the shorter cell shown in the homogeneous case (see Figure 5.3). As a/H is increased, the recirculation zone is successively reduced in size and eventually disappears at the highest a/H value considered (0.25). In addition, the upper wall recirculation zone appears to have been eliminated when the fiber array insert is utilized. The general trends outlined above can be explained in terms of the local influence of the insert on the flow. As the flow moves from the inlet through the insert, the strong resistance to flow causes the streamwise velocity to flatten and spread across the entire duct. The velocity profile near the upper wall is affected first because of the proximity of the inlet, while the spreading of the flow towards the lower wall lags behind. This explains the lengthening of the recirculation zone for low a/H values followed by the elimination of this zone if a/H is large enough. Figure 5.7 illustrates the influence of a lower porosity on the downstream flow field ($\epsilon_f = 0.90$). As expected, the increased

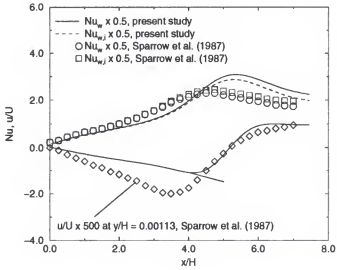

Figure 5.4: Fluid flow in homogeneous duct – Nusselt number and near-wall velocity versus axial location, $Re_H = 600$.

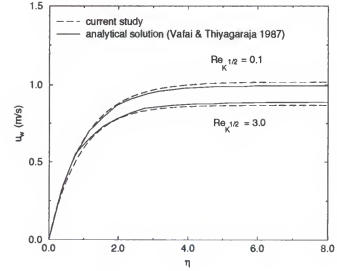

Figure 5.5: Wall velocity versus nondimensional wall coordinate for fully developed porous media flow.

flow resistance causes the lower wall recirculation zone to decrease faster and thus disappear for a shorter segment. Again, the upper recirculation zone cannot be seen in this instance.

Another issue of importance is the influence of Darcy versus non-Darcy modeling assumptions. The previously described figures (Figures 5.6 and 5.7) also feature streamlines for cases where Darcy flow is assumed to be valid regardless of Reynolds number. In general, the flow field is only weakly dependent on these modeling assumptions, as the non-Darcy assumption tends to compute a slightly shorter lower wall recirculation zone because of higher frictional losses. However, there is one notable exception to this trend for $a/H = 0.25$ and a porosity of 0.99 (Figure 5.6(d)): results from Darcy modeling show a small lower wall recirculation zone, which is not seen in the non-Darcy case. This particular combination of a/H and ϵ_f apparently lies near a transition condition, where the downstream flow field changes from recirculating to non-recirculating. As a consequence, the results show marked sensitivity to non-Darcy versus Darcy assumptions.

Quantitative effects of the insert may be shown by examining the streamwise velocity profiles at various locations in the duct. Figures 5.8 and 5.9 illustrate the u velocity profiles at locations one-half and seven duct widths downstream of the step for $a/H = 0.10$ and 0.25. At $x/H = 0.5$ (Figure 5.8), the flattening of the velocity profile can be seen more clearly with an increase in porosity and/or length of the insert. The lowest porosity case (0.90) shows a great deal of deviation from the homogeneous case regardless of the size of the insert. Slight differences can also be seen in Figures 5.8 and 5.9 regarding the non-Darcy versus Darcy modeling assumptions, especially for higher porosities. At $x/H = 7$ (Figure 5.9), the velocity profiles resulting from the insert differ greatly from the homogeneous case since the upper wall recirculation zone is no longer present. As the porosity is reduced and the insert length is expanded, the flow profile tends to approach a fully-developed (parabolic) situation. Non-Darcy and Darcy results also show only slight variation.

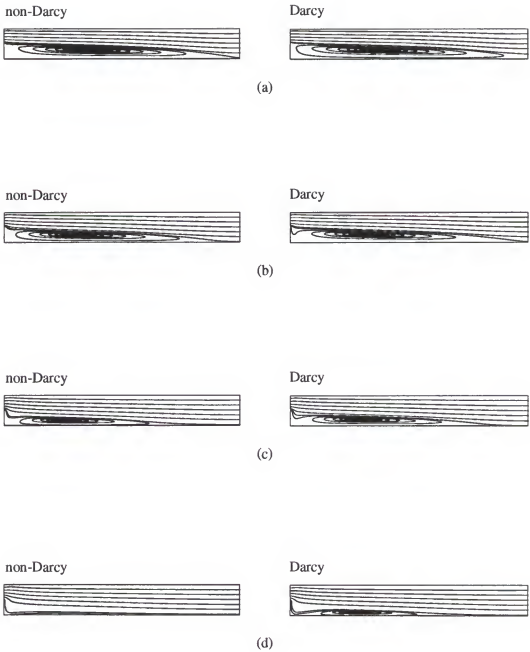

Figure 5.6: Streamline plots, $\epsilon_f = 0.99$ - (a) $a/H = 0.10$; (b) $a/H = 0.15$; (c) $a/H = 0.20$; (d) $a/H = 0.25$.

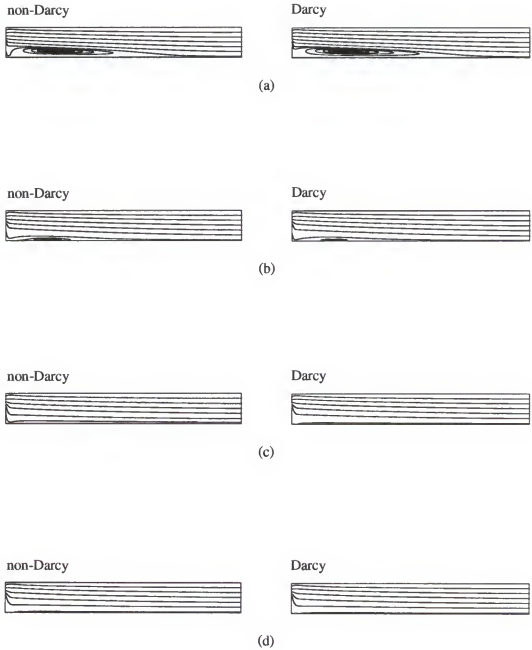

Figure 5.7: Streamline plots, $\epsilon_f = 0.90$ – (a) $a/H = 0.10$; (b) $a/H = 0.15$; (c) $a/H = 0.20$; (d) $a/H = 0.25$.

Results for $\epsilon_f = 0.92$, 0.94, and 0.96 typically lie close to $\epsilon_f = 0.90$ for a given a/H value (for sake of clarity, these cases are not depicted in the figures).

To evaluate the frictional losses resulting from the insert, the head loss, h_l, is calculated for the duct as follows [23]:

$$h_l = \left(\frac{\overline{p}_i}{\rho_f} + \alpha_i \frac{U_i^2}{2}\right) - \left(\frac{\overline{p}_o}{\rho_f} + \alpha_o \frac{U_o^2}{2}\right) \tag{5.6}$$

In this expression, $\overline{p}_i$ and $\overline{p}_o$ are the average inlet and outlet pressures, and α_i and α_o are the kinetic energy coefficients, defined as

$$\alpha_{i,o} = \frac{\int_{A_{i,o}} u^3 dA}{\left(\int_{A_{i,o}} u dA\right)^3} \tag{5.7}$$

Figure 5.10 shows the duct head loss as a function of porosity for the various insert sizes (the head loss is divided by the homogeneous value to yield a dimensionless parameter, h_l^*). Frictional losses are seen to monotonically rise as the porosity is reduced, with a penalty roughly two orders of magnitude larger than the no-insert case when $\epsilon_f = 0.90$. Different combinations of a/H and ϵ_f can result in comparable head loss values, which is most evident at the high porosity end. The minimum head loss value for elimination of the recirculation zone is about four times the homogeneous case, with $a/H = 0.25$ and $\epsilon_f = 0.99$. A comparison between the non-Darcy and Darcy modeling assumptions is also shown on the figure, with only slight differences shown.

5.3 Results – Heat Transfer

Heat transfer performance is shown in Figure 5.11, which features the lower wall Nusselt number, Nu_w (Equation (5.4)), as a function of axial location for the various configurations. For the homogeneous case, a local minimum is shown in Nu_w near the upstream edge of the recirculation zone; further downstream Nu_w reaches a maximum value after reattachment. The addition of the insert causes significant changes in the character of Nu_w for a number of reasons. Since the insert has a large

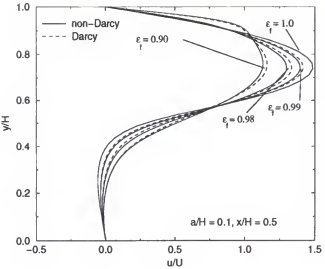

(a)

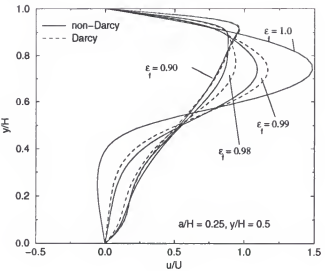

(b)

Figure 5.8: Transverse coordinate versus streamwise velocity component at $x/H = 0.5$ – (a) $a/H = 0.10$; (b) $a/H = 0.25$.

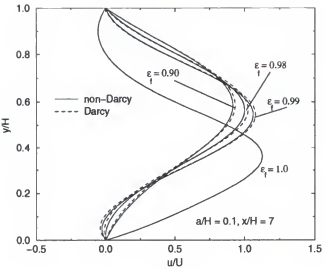

(a)

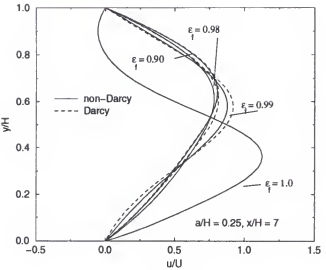

(b)

Figure 5.9: Transverse coordinate versus streamwise velocity component at $x/H = 7$ – (a) $a/H = 0.10$; (b) $a/H = 0.25$.

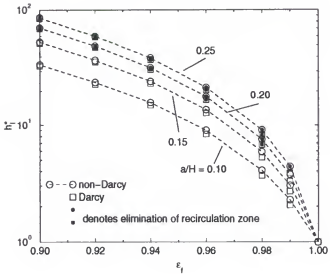

Figure 5.10: Nondimensional duct head loss versus porosity.

conductivity, differences between wall and bulk temperatures are small within this region, resulting in large Nu_w values. For the high porosity case (Figure 5.11(a)), the minimum value of Nu_w near the inlet decreases for $a/H = 0.10$ and 0.15 because of the extension of the lower wall recirculation zone. As a/H is increased, the recirculation zone is reduced in length and consequently the minimum value of Nu_w rises. With regards to the lowest porosity case (Figure 5.11(b)), local minima can be seen near the inlet for $a/H = 0.10$ and 0.15, but not for higher a/H values since there is no recirculation for these cases. Slightly higher values of Nu_w can be seen in Figure 5.11(c), which feature porosities corresponding to the maximum amount of temperature reduction (discussed subsequently). Regardless of the a/H and ϵ_f combination, the Nusselt number near the outlet asymptotically approaches the fully-developed value of 4.12 [6] when the insert is included; flattening of Nu_w at the outlet itself is due to the adiabatic boundary condition.

It is also of interest to quantify the values of maximum wall temperature with and without the insert. Figure 5.12 illustrates the non-dimensionalized maximum

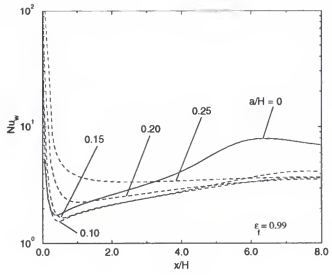

(a)

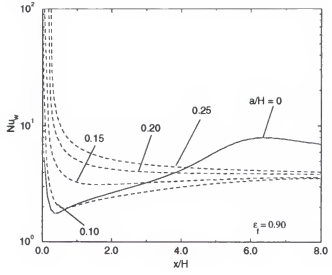

(b)

Figure 5.11: Lower wall Nusselt number versus axial location (non-Darcy, non-LTE modeling assumptions) - (a) $\epsilon_f = 0.99$; (b) $\epsilon_f = 0.90$; (c) ϵ_f selected for optimum temperature reduction.

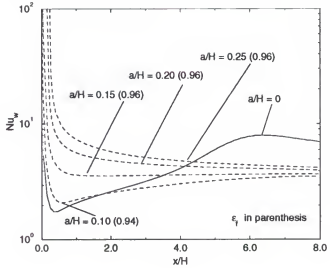

(c)

Figure 5.11: Continued.

wall temperature, T_m^*:

$$T_m^* = \frac{T_m}{T_{m,h}} \tag{5.8}$$

as a function of porosity ($T_{m,h}$ is the maximum wall temperature for the homogeneous case). As demonstrated in the Nusselt number findings, the insert can have a detrimental impact; however, most cases show at least some reduction in wall temperature. The optimum value in temperature reduction with respect to ϵ_f is most apparent for the shorter inserts, with only slight sensitivity to porosity shown at the extreme a/H values. Non-equilibrium thermal conditions (denoted non-LTE) are shown to be important for high porosities and especially for small insert lengths. The value of T_m^* is consistently underpredicted by the LTE assumption, since this condition presumes infinite heat transfer between fluid and fibers. Comparing the non-Darcy versus Darcy flow assumptions, appreciable differences are seen primarily at the high porosity end, where $Re_{\sqrt{K}}$ is typically highest. Results shown in Figure 5.12 can be combined with the head loss values shown in Figure 5.10 in order to

determine the most attractive combination of temperature reduction and frictional penalty. In general, the most equitable tradeoffs are favored for long, highly porous inserts, as opposed those that are short and dense.

5.4 Concluding Remarks

The use of fiber array inserts in recirculating flows has been shown to greatly impact the downstream flow structure, obviously affecting the degree of heat transfer. If the insert is short and highly porous, the lower wall recirculation zone behind the step can be extended, resulting in poorer heat transfer performance with respect to the empty duct. On the other hand, with extension of the insert and/or a decrease in porosity, the recirculation zone is either reduced in size or eliminated altogether. These trends illustrate the need for caution in designing inserts in order to prevent unwanted operating conditions from occurring. The most favorable condition of temperature reduction and head loss penalty is found for an insert of length $a/H = 0.25$ and a porosity of 0.99: the maximum wall temperature is reduced by over 30%, and the head loss is roughly four times higher than the no-fiber case. Beyond this porosity, only incremental wall temperature reductions are possible, accompanied by head losses that approach nearly two orders of magnitude. Non-Darcy effects are more influential at the high porosity end, and in one instance non-Darcy calculations show the disappearance of a recirculation zone which is predicted by Darcy flow. The assumption of local thermodynamic equilibrium is valid only for long inserts, with significant differences appearing for shorter and more porous conditions.

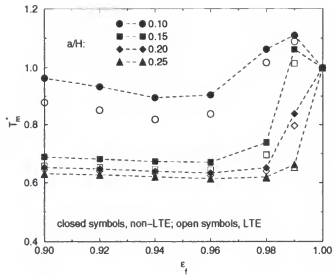

(a)

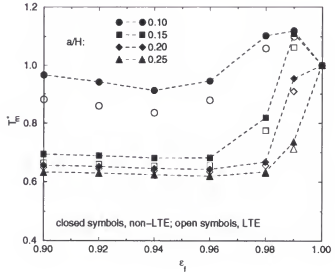

(b)

Figure 5.12: Nondimensionalized maximum wall temperature versus porosity – (a) non-Darcy modeling assumption; (b) Darcy modeling assumption.

CHAPTER 6
CONCLUSIONS

A multiscale modeling procedure has been used to explore heat transfer enhancement with fiber array inserts. The presentation of the macroscopic (porous media) governing equations pointed out the need for microscale investigations in order to determine the exact form of macroscopic source terms appearing in the momentum and energy equations. Microscopic analyses were performed for highly porous square and triangular arrays under low and high laminar Reynolds number conditions, and the results were correlated against the array type, porosity, and flow condition. With the macroscopic source terms specified, fiber array inserts were then considered for a pipe flow application where the insert was installed longitudinal to the tube axis. Nongray radiative transfer was accounted for in this application. An additional application was considered with short inserts placed directly behind a backward-facing step (radiation was not considered here). For both of these applications, deviation from Darcy's law and the importance of the local thermodynamic equilibrium condition were investigated.

A number of conclusions may be drawn from the results presented in this investigation. With regards to the microscale study of flow transverse to square and triangular arrays, frictional losses follow Darcy's law when the Darcian Reynolds number is of the order one; however, significant non-Darcy effects appear at higher Reynolds numbers. Although the chosen numerical procedure cannot resolve very low Reynolds number flows, extrapolation of the results at higher Reynolds numbers can be used to evaluate the frictional losses in this instance. This finding shows that popular computational fluid dynamics (CFD) schemes can be used in

other microscale geometries in order to determine the low flow rate characteristics (such as the permeability) of other porous media. For non-Darcy flows, the Ergun and Forchheimer relations do not correlate well against the results for such high porosity (> 0.80) arrays. The validity of these relationships is thus questionable for porous media which feature large fluid volume fractions. A power-law function based on the porosity and Darcian Reynolds number is developed for each array type to accurately predict frictional losses. Considering heat transfer, Nusselt number correlations based on the particle Reynolds number are also derived via a power-law relationship.

Fiber array inserts placed longitudinally in a circular tube are found to greatly augment the heat transfer rate. For a tube Reynolds number of 1000, silicon carbide (SiC) inserts cause as much as a 30% reduction in tube wall outlet temperature as compared to the no-insert case. The pressure drop penalty increases by an order of ten to one thousand, clearly showing the need for care in evaluating the overall impact of the inserts. Since the flow is aligned parallel to the insert, non-Darcy effects do not appear in this application. Local thermodynamic equilibrium (LTE) conditions are valid for the case of conduction and convection alone, but significant departure from LTE is found when radiation is included. Radiative exchange is largely responsible for the heat transfer augmentation under the conditions studied.

In recirculating flows, the presence of transverse fiber array inserts greatly influences the flow structure and hence the degree of heat transfer. For the flow over a backward-facing step, short and highly porous inserts cause the lower wall recirculation zone to increase in length, which deteriorates heat transfer performance with respect to the empty duct. Conversely, the recirculation zone can either be reduced in size or be completely eliminated with longer and less porous inserts. Much like the pipe flow application, extreme care in the design process is warranted so that unwanted operating conditions can be avoided. With respect to the given conditions, the maximum wall temperature is reduced by over 30% with an insert having

a length to duct height ratio of 0.25 and a porosity of 0.99; the head loss penalty increases by a factor of four over the no-fiber case. At higher porosities and longer insert lengths, wall temperatures are reduced by only small fractions, while the head losses gain nearly two orders of magnitude. Non-Darcy effects appear mostly at high porosities, and in one circumstance non-Darcy calculations show the disappearance of a recirculation zone predicted by Darcy flow. Deviation from LTE is most evident for highly porous and short inserts.

The relatively large reduction in wall temperatures seen in the above applications demonstrates the potential for heat transfer augmentation and cost savings with fiber array inserts. Based on the positive performance that is exhibited by the inserts, experimental studies are warranted at this stage. Aside from determining insert performance under more realistic conditions, methods for constructing and installing actual fiber array inserts can be developed and tested. In addition, experimental results can be used to check the validity of the theoretical modeling approach and the assumptions taken. Future theoretical modeling should focus more closely on turbulent flow aspects, as they are important in a multitude of engineering applications. Similarly, the treatment of non-periodic microscopic geometries and flow conditions should be addressed. For such cases, the development of effective and efficient schemes which couple macro- and microscale phenomena is a primary objective. Engineers and scientists have much knowledge to gain as the capabilities of multiscale modeling continue to grow.

REFERENCES

[1] B. Abu-Hijleh. Convection heat transfer from a laminar flow over a 2-d backward facing step with asymmetric and orthotropic porous floor segments. *Numerical Heat Transfer, Part A*, 31:325–335, 1997.

[2] A. Amiri and K. Vafai. Analysis of dispersion effects and non-thermal equilibrium, non-darcian, variable porosity incompressible flow through porous media. *International Journal of Heat and Mass Transfer*, 37(6):939–954, 1994.

[3] B. Åström, R. Pipes, and S. Advani. On flow through aligned fiber beds and its application to composites processing. *Journal of Composite Materials*, 26(9):1351–1373, 1992.

[4] J. Bear. *Dynamics of Fluids in Porous Media.* Dover, New York, 1988.

[5] G. Beavers and E. Sparrow. Non-darcy flow through fibrous porous media. *Journal of Applied Mechanics*, 36:711–714, 1969.

[6] A. Bejan. *Convective Heat Transfer.* Wiley-Interscience, New York, 2nd edition, 1995.

[7] A.E. Bergles. Techniques to augment heat transfer. In W. M. Rosenhow, J. P. Hartnett, and E. N. Ganic, editors, *Handbook of Heat Transfer Applications*, pages 3.1–3.80. McGraw-Hill, New York, 2nd edition, 1985.

[8] R. B. Bird, W. E. Stewart, and E. N. Lightfoot. *Transport Phenomena.* Wiley, New York, 1960.

[9] C. Bohren and D. Huffman. *Absorption and Scattering of Light by Small Particles.* Wiley-Interscience, New York, 1983.

[10] J. C. Chai. *A Finite-Volume Method for Radiation Heat Transfer.* Ph.D. Dissertation, University of Minnesota, 1994.

[11] J. C. Chai, H. S. Lee, and S. V. Patankar. Finite volume method for radiation heat transfer. *AIAA Journal of Thermophysics and Heat Transfer*, 1994(3):419–425, 1994.

[12] P. Cheng. Heat transfer in geothermal systems. *Advances in Heat Transfer*, 14:1–105, 1978.

[13] E. H. Chui, G. D. Raithby, and P. M. J. Hughes. Prediction of radiative transfer in cylindrical enclosures with the finite volume method. *Journal of Themophysics and Heat Transfer*, 6(4):605–611, 1992.

[14] D. S. Clague and R. J. Phillips. A numerical calculation of the hydraulic permeability of three-dimensional disordered fibrous media. *Physics of Fluids*, 9(6):1562–1572, 1997.

[15] T. F. Cooke. Inorganic fibers – a literature review. *Journal of the American Ceramic Society*, 74(12):2959–2978, 1991.

[16] J. Drummond and M. Tahir. Laminar viscous flow through regular arrays of parallel solid cylinders. *Journal of Multiphase Flow*, 10(5):515–540, 1984.

[17] R. Echigo. Effective energy conversion method between gas enthalpy and thermal radiation and application to industrial furnaces. In *Proceedings of the 7th International Heat Transfer Conference*, volume VI, pages 361–366, Munich, 1982.

[18] R. Echigo, Y. Yoshizawa, K. Hanamura, and T. Tomimura. Analytical and experimental studies on radiative propagation in porous media with internal heat generation. In *Proceedings of the 8th International Heat Transfer Conference*, volume II, pages 827–832, San Francisco, 1986.

[19] D. A. Edwards, M. Shapiro, P. Bar-Yoseph, and M. Shapira. The influence of reynolds number upon the apparent permeability of spatially periodic arrays of cylinders. *Physics of Fluids*, 2(1):45–55, 1990.

[20] T. Einstein. Radiant heat transfer to absorbing gases enclosed in a circular pipe with conduction, gas flow, and internal heat generation. NASA Technical Report TR-156, NASA, 1963.

[21] S. Ergun. Fluid flow through packed columns. *Chemical Engineering Progress*, 48(2):89–94, 1952.

[22] W.A. Farone and C.W. Querfeld. Electromagnetic scattering from radially inhomogeneous infinite cylinders at oblique incidence. *Journal of the Optical Society of America*, 56:476–480, 1966.

[23] R. W. Fox and A. T. McDonald. *Introduction to Fluid Mechanics*. Wiley, New York, 4th edition, 1992.

[24] D. K. Gartling. A test problem for outflow boundary conditions – flow over a backward-facing step. *International Journal for Numerical Methods in Fluids*, 11:953–967, 1990.

[25] C. K. Ghaddar. On the permeability of unidirectional fibrous media: A parallel computational approach. *Physics of Fluids*, 7(11):2563–2586, 1995.

[26] W. G. Gray. A derivation of the equations for multi-phase transport. *Chemical Engineering Science*, 30:229–233, 1975.

[27] R. C. Hendricks, M. J. Braun, V. Canacci, and R. L. Mullen. Simulation of brush insert for leading-edge-passage convective heat transfer. In *Fourth International Symposium in Transport Phenomena*, Sydney, 1991.

[28] H. Hiraoka. Modelling of turbulent flows within plant/urban canopies. *Journal of Wind Engineering and Industrial Aerodynamics*, 46 & 47:173–182, 1993.

[29] P. C. Huang and K. Vafai. Analysis of forced convection enhancement in a channel using porous blocks. *Journal of Thermophysics and Heat Transfer*, 8(3):563–573, 1994.

[30] K. Ichimiya, T. Matsuda, and Y. Kawai. Effects of a porous medium on local heat transfer and fluid flow in a forced convection field. *International Journal of Heat and Mass Transfer*, 40(7):1567–1576, 1997.

[31] K. H. Im and R. K. Ahluwalia. Radiative enhancement of tube-side heat transfer. *International Journal of Heat and Mass Transfer*, 37(17):2635–2646, 1994.

[32] F. Incropera and D. DeWitt. *Fundamentals of Heat and Mass Transfer*. John Wiley, New York, 2nd edition, 1985.

[33] M. Kaviany and B. P. Singh. Radiative heat transfer in porous media. *Advances in Heat Transfer*, 23:133–186, 1993.

[34] H. H. Krause, D. A. Vaughan, P. W. Cover, W. K. Boyd, and D. A. Oberacker. Corrosion and deposits from combustion of solid waste. *Journal of Engineering for Power*, 99:449–459, 1977.

[35] S. C. Lee. Effect of fiber orientation on thermal radiation in fibrous media. *International Journal of Heat and Mass Transfer*, 32(2):311–319, 1989.

[36] T. Masuoka and Y. Takatsu. Turbulence model for flow through porous media. *International Journal of Heat and Mass Transfer*, 39(13):2803–2809, 1996.

[37] C. Mendoza and D. Zhou. Effects of porous beds on turbulent stream flow above bed. *Journal of Hydraulic Engineering*, 118(9):1222–1240, 1992.

[38] J.P. Moder, J. C. Chai, G. Parthasarathy, H. S. Lee, and S. V. Patankar. Nonaxisymmetric radiative transfer in cylindrical enclosures. *Numerical Heat Transfer, Part B*, 30(4):437–452, 1996.

[39] M. Modest. *Radiative Heat Transfer*. McGraw-Hill, New York, 1993.

[40] R.V. Morgan. The overall convective heat transfer from smooth circular cylinders. *Advances in Heat Transfer*, 11:199–263, 1975.

[41] R. G. Munro and S. J. Dapkunas. Corrosion characteristics of silicon carbide and silicon nitride. *Journal of Research of the National Institute of Standards and Technology*, 98(5):607–631, 1993.

[42] S. R. Nutt and F. E. Wawner. Silicon carbide filaments: Microstructure. *Journal of Materials Science*, 20:1953–1960, 1985.

[43] E. Palik. *Handbook of Optical Constants of Solids II*. Academic Press, Orlando, 1985.

[44] S. V. Patankar. *Numerical Heat Transfer and Fluid Flow*. Hemisphere, New York, 1980.

[45] S. V. Patankar, C. H. Liu, and E. M. Sparrow. Fully developed flow and heat transfer in ducts having streamwise-periodic variations of cross-sectional area. *Journal of Heat Transfer*, 99:180–186, 1977.

[46] A. S. Sangani and A. Acrivos. Slow flow past periodic arrays of cylinders with application to heat transfer. *International Journal of Multiphase Flow*, 8(3):193–206, 1982.

[47] L. L. Shreir. *Corrosion*. Newnes-Butterworths, Boston, 1976.

[48] W. Shyy. *Computational Modeling for Fluid Flow and Interfacial Transport.* Elsevier Science Publishers, Amsterdam, 1994.

[49] W. Shyy, S. Thakur, H. Ouyang, J. Liu, and E. Blosch. *Computational Techniques for Complex Transport Phenomena.* Cambridge University Press, New York, 1997.

[50] W. Shyy and T. Vu. Modeling and computation of flow in a passage with 360-degree turning and multiple airfoils. *Journal of Fluids Engineering*, 115:103–108, 1993.

[51] R. Siegel and J. R. Howell. *Thermal Radiation Heat Transfer.* Hemisphere, Washington, 3rd edition, 1992.

[52] J. C. Slattery. *Momentum, Energy, and Mass Transfer in Continua.* McGraw-Hill, New York, 1971.

[53] E. M. Sparrow, S. S. Kang, and W. Chuck. Relation between the points of flow reattachment and maximum heat transfer for regions of flow separation. *International Journal of Heat and Mass Transfer*, 30(7):1237–1246, 1987.

[54] E. M. Sparrow, A. L. Loeffler, and H. A. Hubbard. Heat transfer to longitudinal laminar flow between cylinders. *Journal of Heat Transfer*, 83:415–422, 1961.

[55] S. Thakur, J. Wright, W. Shyy, J. Liu, H. Ouyang, and T. Vu. Development of pressure-based composite multigrid methods for complex fluid flows. *Progress in Aerospace Sciences*, 32:313–375, 1996.

[56] H. Thielsch and F. M. Cone. Corrosion in recovery and refuse-fired boilers. In *Proceedings of the 1994 International Joint Power Generation Conference*, Kansas City, MO, 1994.

[57] C.-L. Tien and K. Vafai. Convective and radiative heat transfer in porous media. *Advances in Applied Mechanics*, 27:225–281, 1990.

[58] C.L. Tien. Thermal radiation in packed and fluidized beds. *ASME Journal of Heat Transfer*, 110:1230–1241, 1988.

[59] V. Travkin and I. Catton. A two-temperature model for turbulent flow and heat transfer in a porous layer. *Journal of Fluids Engineering*, 117:181–188, 1995.

[60] V. Travkin, I. Catton, and L. Gratton. Single phase turbulent transport in prescribed non-isotropic and stochastic porous media. In *Heat Transfer in Porous Media*, volume 240 (HTD), pages 43–48, 1993.

[61] K. Vafai and P. C. Huang. Analysis of heat transfer regulation and modification employing intermittently emplaced porous cavities. *Journal of Heat Transfer*, 116:604–613, 1994.

[62] K. Vafai and M. Sözen. Analysis of energy and momentum transport for fluid flow through a porous bed. *Journal of Heat Transfer*, 112:690–699, 1990.

[63] K. Vafai and R. Thiyagaraja. Analysis of flow and heat transfer at the interface region of a porous medium. *International Journal of Heat and Mass Transfer*, 30(7):1391–1405, 1987.

[64] H.C. van de Hulst. *Light Scattering by Small Particles.* Dover Publications, New York, 1981.

[65] O. van Genabeek and D. H. Rothman. Macroscopic manifestations of microscopic flows through porous media: Phenomenology from simulation. *Annual Review of Earth and Planetary Sciences*, 24:63–87, 1996.

[66] K.Y. Wang, S. Kumar, and C.L. Tien. Radiative transfer in thermal insulations of hollow and coated fibers. *AIAA Journal of Thermophysics and Heat Transfer*, 1(4):289–295, 1987.

[67] S. Whitaker. Advances in theory of fluid motion in porous media. *Industrial and Engineering Chemistry*, 61(12):14–28, 1969.

[68] J. M. Zhang, W. H. Sutton, and F. C. Lai. Enhancement of heat transfer using porous convection-to-radiation converter for laminar flow in a circular duct. *International Journal of Heat and Mass Transfer*, 40(1):39–48, 1997.

[69] D. Zhou and C. Mendoza. Flow through porous bed of turbulent stream. *Journal of Hydraulic Engineering*, 119(2):365–383, 1993.

[70] A. Žukauskas. Convective heat transfer in cross flow. In S. Kakaç, R. K. Shah, and W. Aung, editors, *Handbook of Single-Phase Convective Heat Transfer*, pages 6.1–6.45. Wiley, New York, 1987.

[71] A. Žukauskas. Heat transfer from tubes in crossflow. *Advances in Heat Transfer*, 18:87–159, 1987.

[72] A. Žukauskas and R. Ulinskas. Banks of plain and finned tubes. In G. F. Hewitt, editor, *Hemisphere Handbook of Heat Exchanger Design*, pages 2.2.4–1 – 2.2.4–17. Hemisphere, New York, 1990.

BIOGRAPHICAL SKETCH

Andrew Read Martin was born on November 27, 1968, in Manhasset, New York, but has lived in Florida since 1975. He entered the University of Florida as an undergraduate student in 1986, not knowing that his days as a college student would span over one decade. In 1991 he earned a Bachelor of Science in Mechanical Engineering degree, and two years later earned a Master of Science degree from the same university. While working as a graduate assistant, the author had the great fortune of meeting Viktoria Öberg, a Chemical Engineering graduate student visiting from Sweden with an exchange program. The two became a close couple in 1992 and eventually married in 1996. After realizing that no higher a degree could be obtained, the author's career as a professional student came to a close in 1997 with the degree of Doctor of Philosophy. After graduation, the author will begin his next adventure as a post-doctoral researcher at the Royal Institute of Technology in Stockholm, Sweden.

I certify that I have read this study and that in my opinion it conforms to acceptable standards of scholarly presentation and is fully adequate, in scope and quality, as a dissertation for the degree of Doctor of Philosophy.

Craig J. Saltiel, Chair
Assistant Professor of Mechanical Engineering

I certify that I have read this study and that in my opinion it conforms to acceptable standards of scholarly presentation and is fully adequate, in scope and quality, as a dissertation for the degree of Doctor of Philosophy.

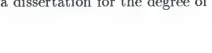

Wei Shyy, Cochair
Professor of Aerospace Engineering, Mechanics and Engineering Science

I certify that I have read this study and that in my opinion it conforms to acceptable standards of scholarly presentation and is fully adequate, in scope and quality, as a dissertation for the degree of Doctor of Philosophy.

James F. Klausner
Associate Professor of Mechanical Engineering

I certify that I have read this study and that in my opinion it conforms to acceptable standards of scholarly presentation and is fully adequate, in scope and quality, as a dissertation for the degree of Doctor of Philosophy.

William E. Lear Jr.
Assistant Professor of Mechanical Engineering

I certify that I have read this study and that in my opinion it conforms to acceptable standards of scholarly presentation and is fully adequate, in scope and quality, as a dissertation for the degree of Doctor of Philosophy.

Renwei Mei
Associate Professor of Aerospace Engineering, Mechanics and Engineering Science

This dissertation was submitted to the Graduate Faculty of the College of Engineering and to the Graduate School and was accepted as partial fulfillment of the requirements for the degree of Doctor of Philosophy.

December 1997

Winfred M. Phillips
Dean, College of Engineering

Karen A. Holbrook
Dean, Graduate School